A Numerical Study of the Impact of Vertical Shear on the Distribution of Rainfall in Hurricane Bonnie (1998)

ROBERT ROGERS

Cooperative Institute for Marine and Atmospheric Studies, Rosenstiel School for Marine and Atmospheric Science, University of Miami, Miami, Florida

SHUYI CHEN AND JOSEPH TENERELLI

Rosenstiel School for Marine and Atmospheric Science, University of Miami, Miami, Florida

HUGH WILLOUGHBY

NOAA/AOML/Hurricane Research Division, Miami, Florida

(Manuscript received 30 January 2002, in final form 29 August 2002)

ABSTRACT

Despite the significant impacts of torrential rainfall from tropical cyclones at landfall, quantitative precipitation forecasting (QPF) remains an unsolved problem. A key task in improving tropical cyclone QPF is understanding the factors that affect the intensity and distribution of rainfall around the storm. These include the storm motion, topography, and orientation of the coast, and interactions with the environmental flow. The combination of these effects can produce rainfall distributions that may be nearly axisymmetric or highly asymmetric and rainfall amounts that range from 1 or 2 cm to >30 cm.

This study investigates the interactions between a storm and its environmental flow through a numerical simulation of Hurricane Bonnie (1998) that focuses on the role of vertical wind shear in governing azimuthal variations of rainfall. The simulation uses the high-resolution nonhydrostatic fifth-generation Pennsylvania State University–NCAR Mesoscale Model (MM5) to simulate the storm between 0000 UTC 22 August and 0000 UTC 27 August 1998. During this period significant changes in the vertical shear occurred in the simulation. It changed from strong west-southwesterly, and across track, to much weaker south-southwesterly, and along track. Nearly concurrently, the azimuthal distribution of convection changed from a distinct wavenumber-1 pattern to almost azimuthally symmetric by the end of the time period. The strongest convection in the core was generally located on the downshear left side of the shear vector when the shear was strong. The azimuthal distributions and magnitudes of low-level radial inflow, reflectivity, boundary layer divergence, and low-level vertical motion all varied consistently with the evolution of the vertical shear. Additionally, the vortex showed a generally downshear tilt from the vertical. The magnitude of the tilt correlated well with changes in magnitude of the environmental shear. The accumulated rainfall was distributed symmetrically across the track of the storm when the shear was strong and across track, and it was distributed asymmetrically across the track of the storm when the shear was weak and along track.

1. Introduction

a. Background of studies involving the distribution of rainfall in tropical cyclones

Despite significant impacts of heavy rainfall that often accompany tropical cyclone landfall, quantitative precipitation forecasting (QPF) remains a challenge. Freshwater flooding associated with landfalling tropical cyclones has been responsible for more than half of all the deaths caused by tropical cyclones in the United States over the last 30 years (Rappaport et al. 1999). Rainfall measured at a particular location during the passage of a tropical cyclone depends on many factors: location with respect to the storm's track, the maximum intensity and storm-relative distribution of rainfall, storm translational speed, and local effects such as topography and orientation of the coast. Consequently, precipitation can vary greatly from storm to storm and even over time during the same storm.

Despite the clear threat from tropical cyclone rainfall, forecasting techniques remain crude. For example, a well-known rule of thumb for forecasting the amount of rainfall that occurs from a tropical cyclone is based on a simple empirical formula that considers only the

Corresponding author address: Dr. Robert Rogers, Cooperative Institute for Marine and Atmospheric Studies, Rosenstiel School for Marine and Atmospheric Science, University of Miami, 4600 Rickenbacker Cswy., Miami, FL 33149.
E-mail: rogers@aoml.noaa.gov

translational speed of the storm. Clearly the improvement of QPF should be a top priority and, as pointed out by Marks et al. (1998), tropical cyclones provide an ideal environment for testing and improving QPF techniques. A key task leading to such improvements is developing a better understanding of the processes that affect the intensity and distribution of rainfall. Such processes can combine to produce rainfall distributions that range from nearly axisymmetric to highly asymmetric and rainfall amounts that range from minimal to catastrophic.

Most of the studies of the intensity and distribution of rainfall around a storm have focused on the translational speed of the storm and the interaction of the storm with environmental vertical wind shear. Examples of studies that have focused on the movement of storms in governing the azimuthal distribution of convection include Shapiro (1983) and Peng et al. (1999). Shapiro (1983) used a boundary layer model to investigate the development of azimuthal asymmetries in patterns of frictionally induced boundary layer convergence as a function of the translational speed of a tropical cyclone. He found that for slow-moving systems (<5 m s^{-1}) convergence is strongest ahead of the storm, while for fast-moving systems (>10 m s^{-1}) convergence becomes concentrated more ahead and to the right of the storm. Peng et al. (1999), using a primitive equation mesoscale model, found that asymmetries created by the translation can lead to a decoupling between the regions of maximum surface fluxes and maximum low-level convergence, reducing the intensity of the storms.

It has long been recognized that shear is detrimental to the formation and maintenance of tropical cyclones (e.g., Gray 1968; DeMaria 1996). Shear is also associated with azimuthal asymmetries in the vertical motion, convergence, and rainfall fields. Several observationally based studies have shown that inner-core convection and rainfall tends to become organized on the left side of the shear vector when looking downshear (Willoughby et al. 1984; Marks et al. 1992; Franklin et al. 1993; Gamache et al. 1997; Corbosiero and Molinari 2002; Black et al. 2002). The conceptual model that has arisen from these studies is that updrafts are initiated downshear, are wrapped cyclonically around the core by the rapidly rotating tangential winds, and create a maximum vertical motion in the downshear left quadrant. Maximum precipitation is displaced farther counterclockwise through advection.

Willoughby et al. (1984) proposed that a pattern of low-level convergence and divergence was produced on opposite sides of the eyewall of Hurricane Gert of 1981 by differential vorticity advection created by vertical shear. Bender (1997) performed an idealized simulation of Hurricane Gilbert (1998) using the Geophysical Fluid Dynamics Laboratory (GFDL) hurricane model to show that relative flow (i.e., vertical shear) across the storm is also created by beta gyres associated with the advection of planetary vorticity by the symmetric component of the vortex. This relative flow creates differential vorticity advection, leading to the development of azimuthal asymmetries in low-level convergence, upward motion, and convection in the core.

Other studies have viewed the development of azimuthal asymmetries as a result of shear-induced tilt of the vortex. Jones (1995, 2000) performed numerical simulations using a dry primitive equation model of barotropic and baroclinic vortices on an f plane. These vortices initially developed a tilt in the direction of the vertical shear vector. The vertical penetration of the potential vorticity anomalies associated with the tilted vortex induces weak upward motion downshear and downward motion upshear that creates cold anomalies downshear and warm anomalies upshear. Since the model does not contain latent heat release, the air flows isentropically with the primary circulation of the cyclone. Upward motion is strongest in the downshear-right quadrant, as the air ascends the cold anomaly there, and downward motion is maximized in the upshear-left quadrant, as the air descends the warm anomaly there. Over time, the induced circulations cause the axis of tilt of the vortex to rotate, carrying the vertical motion asymmetries with it. Properties of the tilted vortex, such as magnitude of the tilt and rotation rate of the vortex axis, change as properties that determine the Rossby penetration depth, such as static stability, vortex size and strength, and Coriolis parameter, are varied.

Using a dry version of the fifth-generation Pennsylvania State University–National Center for Atmospheric Research (Penn State–NCAR) Mesoscale Model (MM5; Grell et al. 1994), Frank and Ritchie (1999) produced a behavior similar to that shown by Jones (1995) in environmental shears ranging between 5 and 15 m s^{-1} between 850 and 200 hPa. They simulated the development of low-level upward motion in the downshear-right quadrant and downward motion in the upshear-left quadrant. However, when moisture (and diabatic processes) was included in the model (Frank and Ritchie 2001), the development of the low-level temperature anomalies by vertical motion did not occur in the core because the air was saturated there. Rather, upward motion was strongest in the downshear-left quadrant. Furthermore, their simulations showed that the vortex did not develop an appreciable tilt until *after* significant asymmetries had already developed in tangential winds, low-level convergence, and upward motion. They attributed the development of these asymmetries in their simulations to outward horizontal eddy fluxes of equivalent potential temperature and potential vorticity induced by relative flow through the storm.

Detailed, high-resolution analysis of the observed vorticity structure of the inner core of Hurricane Olivia (1994) using airborne dual-Doppler radar were performed by Reasor et al. (2000). During the time of their analysis (a 3.5-h time period) the storm experienced an increase in vertical wind shear, from <5 m s^{-1} between 0.75 and 10.5 km to about 15 m s^{-1}. Simultaneously

the reflectivity changed from primarily axisymmetric to a significant wavenumber-1 asymmetry. Using a simplex method (Neldar and Mead 1965) for locating the storm center at various vertical levels, they found that the tilt of the vortex was basically zero while the shear was low, and increased to about 3 km between 0.75 and 6 km as the shear increased. The direction of the calculated tilt was roughly downshear. While this magnitude of tilt is relatively small, it contrasts with the findings of Frank and Ritchie (2001), who found that the tilt was not detectable in their model until after asymmetries had developed. Furthermore, since the motion of Olivia was mostly constant during the 3.5 h covered by the radar analysis, changes in the distribution of convection likely were not attributable to changes in storm-motion-induced boundary layer convergence patterns. Although this analysis could not definitively isolate the relevant mechanisms governing the development of the azimuthal asymmetries, Reasor et al. indicate that the most likely cause of the asymmetries was the downward projection of the potential vorticity associated with the tilted vortex in the presence of vertical shear.

b. Overview of current study

This study reports a numerical simulation of Hurricane Bonnie (1998) that is performed to investigate the role that vertical shear plays in governing the distribution of rainfall in the core of the storm. The high-resolution, fully nonlinear, nonhydrostatic numerical model (MM5) is used to simulate the storm during a 120-h time period. During the time period covered by the simulation, the storm was observed to undergo considerable changes in the azimuthal distribution of convection, changing from a highly asymmetric, wavenumber-1 pattern when the environmental shear was strong to a more symmetric reflectivity pattern when the shear was weaker. The domains used provided high resolution (minimum grid length of 1.67 km) during the final 48 h of the simulation, when the shear over the storm weakened and the reflectivity distribution became more symmetric. High resolution is essential to resolve convection explicitly and determine such parameters as vortex tilt.

The main purpose of this paper is to document the simulation in comparison with best track data, airborne radar reflectivity fields, and model analysis fields; to show the development of azimuthal asymmetries; and to examine how they correlate with the changes in the vertical shear encountered by the storm. Section 2 contains a description of the model used here, while section 3 contains a brief overview of Hurricane Bonnie. Section 4 presents the results of the simulation, including the evolution of convective asymmetries in the context of changing vertical wind shear. Section 5 explores the likely mechanisms, while section 6 provides a summary and concluding remarks. Detailed examinations of the mechanisms underlying the development of these asymmetries will appear in a forthcoming paper.

2. Description of model

a. Model configuration

The version of MM5 used here (Grell et al. 1994) has been well documented and used in a wide variety of applications, including tropical cyclone simulations (e.g., Liu et al. 1997; Braun and Tao 2000). The 120-h simulation reported here uses four domains: an outer mesh with a grid length of 45 km and three nested inner meshes, all with two-way interactions, having grid lengths of 15, 5, and 1.67 km (Fig. 1). The outer domain size is 86×86 grid points, while the three inner meshes each have domain sizes of 160×160. All domains have 29 vertical levels. The initial fields are obtained from 1° National Centers for Environmental Prediction (NCEP) analyses taken from the Aviation (AVN) Model. The simulation begins at 0000 UTC 22 August 1998, when the storm first became a hurricane with minimum sea level pressure of about 990 hPa. Only the two outermost meshes are used for the first 24 h. After 24 h, the third mesh (5-km grid length) is initialized from the 15-km mesh and run concurrently. After 72 h of total simulation time, the innermost mesh (1.67-km grid length) is initialized from the 5-km mesh and run for the final 48 h of simulation time.

Precipitation processes on the grid scale are represented with an explicit moisture scheme that includes predictive equations for cloud water, cloud ice, rain, and snow (Dudhia 1989). This scheme is used on all four meshes. A high-resolution planetary boundary layer (PBL) parameterization (Zhang and Anthes 1982) is used to simulate the vertical mixing of temperature, water vapor, momentum, and cloud water. The parameterization uses a surface energy budget that is based on the force–restore method developed by Blackadar (1979). This budget is dependent on the surface sensible and latent heat fluxes, substrate fluxes, and radiative fluxes. Over water, roughness lengths, which are used to determine surface exchange coefficients, are based on the friction velocity using the Charnock relationship (Delsol et al. 1971). Sea surface temperatures are based on the initial analysis fields from NCEP and are held constant throughout the simulation. While it would be preferable to vary sea surface temperature to allow for an oceanic response to the strong winds at the surface, such an atmosphere–ocean–wave coupled model is not presently available. Furthermore, several other simulations of tropical cyclones (e.g., Liu et al. 1997; Braun and Tao 2000) hold sea surface temperature fixed in time. Until a fully coupled model is developed and tested, the procedure of holding sea surface temperatures constant will be followed here. Both short- and longwave radiative effects are accounted for where clouds are explicitly represented in the model. Surface radiative fluxes are provided by the scheme used here (Dudhia 1989). To represent deep, moist convection in the model, the Kain–Fritsch parameterization scheme (Kain and Fritsch 1993) is used on the two outermost meshes. This

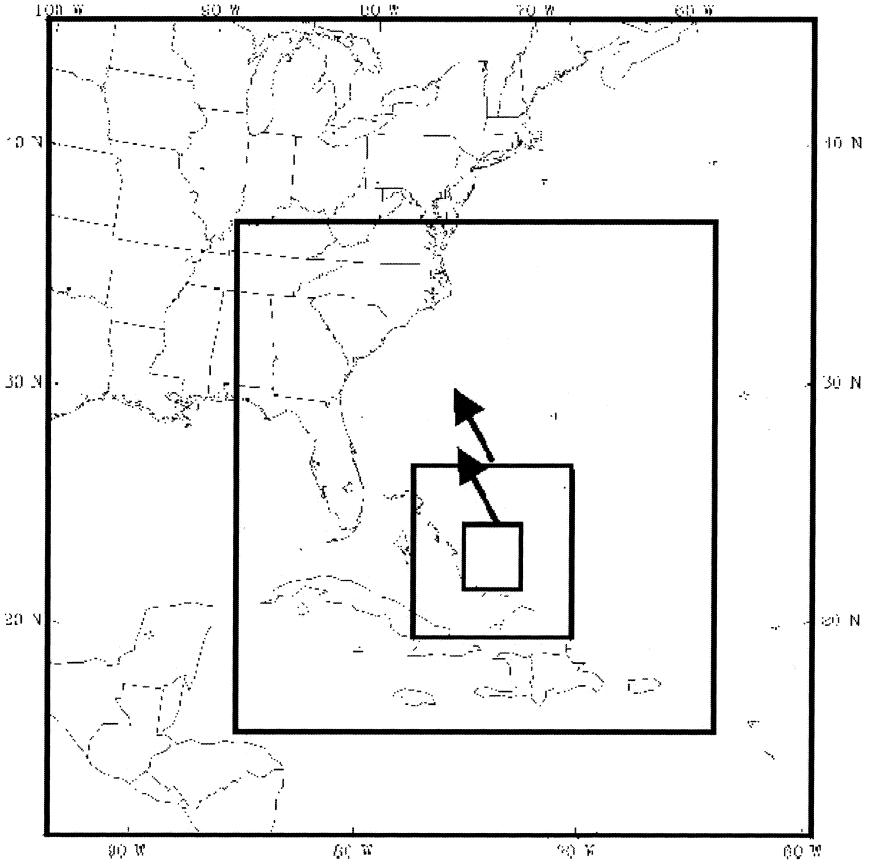

FIG. 1. Domains used in this simulation, with grid lengths of 45, 15, 5, and 1.67 km. Inner two meshes move with the storm.

scheme employs a relatively sophisticated mass-flux cloud model to determine entrainment and detrainment rates as a function of the local (grid element) environment, and it includes the effects of moist downdrafts. On the two innermost meshes, no convective parameterization scheme is used.

On the outermost mesh, four-dimensional data assimilation (FDDA; Stauffer and Seaman 1990; Grell et al. 1994) is used to nudge the wind and temperature fields toward the analysis fields during the first 72 h of the simulation. Four-dimensional data assimilation has been shown to significantly improve simulations when observations are sparse. In this case FDDA is used to improve the simulated track of the storm, since a better representation of the track will better depict the environmental flow fields and sea surface temperatures experienced by the storm and the effect of land—all factors that could impact the distribution of rainfall in the storm. Using FDDA on the higher-resolution meshes would hamper the model's ability to develop finescale structures necessary for the maintenance of the storm. Many tropical cyclone simulations conducted in research mode (e.g., Liu et al. 1997; Braun and Tao 2000) use analysis fields from global models as lateral boundary conditions (LBCs) on the outermost mesh. Since FDDA was not used on the inner meshes in this simulation, the use of FDDA on the outer mesh for the purpose of improving the lateral boundary conditions for the domains containing the storm is not fundamentally different than the other simulations; the only difference is that the lateral boundary conditions are provided from the outermost MM5 domain rather than the global model analysis fields. The technique of using FDDA on the outer mesh only has been used in other modeling studies to improve the LBCs for the inner meshes (e.g., Chen et al. 2001). After 72 h, FDDA is stopped on the outermost mesh.

A unique aspect of this simulation compared to other tropical cyclone simulations using MM5 is the use of an automated movable fine mesh (Tenerelli and Chen 2000). This scheme, similar to the one used in the GFDL hurricane model (Kurihara et al. 1995), permits the specification of a high-resolution mesh that moves with the cyclone, allowing for longer high-resolution simulations than would be possible with a fixed mesh. In the scheme, an algorithm for determining the approximate center of the storm in the parent mesh (in this case the location of the 500-hPa geopotential height minimum) is used. Once this location is determined, the center of the high-resolution mesh is moved to the storm center. The location of the cyclone is checked every hour and the

mesh is moved accordingly. As the mesh is moved, state variables near the boundaries are interpolated from the parent mesh. The choice of 1 h as the update time period was made as a compromise between minimizing interpolation errors and minimizing the costs of grid-shifting. The movable-mesh scheme was used for the 5- and 1.67-km meshes.

b. Center-defining algorithm and wind field decomposition

To evaluate the environmental shear and monitor changes in the vortex structure, the vortex center must be accurately located in order to decompose the wind field into the background flow and the vortex itself. In a manner similar to that described in Marks et al. (1992), the position of the storm center is assumed to vary with height, on the assumption that the environmental flow distorts the vortex shape. This procedure projects ''pseudomode'' (e.g., Michalke and Timme 1967) asymmetries onto the vertically varying vortex position rather than an explicit asymmetry about a common center at all levels (Willoughby 1988).

To locate the vortex center, a technique similar to the simplex algorithm (Neldar and Mead 1965; Marks et al. 1992) is used to find the location at each level where the total tangential wind component taken in a radial band centered on the radius of maximum winds is greatest. This procedure finds the location where the eyewall vorticity is greatest.

The vortex winds can then be Fourier decomposed into azimuthally averaged (i.e., symmetric) and asymmetric fields, as is done in studies using airborne Doppler radar to study hurricane inner-core structures (e.g., Marks et al. 1992; Reasor et al. 2000). The horizontal storm-relative wind, $\mathbf{v}_s$, can be expressed as

$$\mathbf{v}_s(x, y, z) = \mathbf{v}(x, y, z) - \mathbf{v}_c, \tag{1}$$

where $\mathbf{v}$ is the total (model generated) wind and $\mathbf{v}_c$ is the storm motion vector (a spatial constant defined by an objective fit to the trajectory of the minimum sea level pressure). The total storm-relative wind, $\mathbf{v}_s$, can be divided into a horizontally averaged component and the deviation from that component:

$$\mathbf{v}_s(x, y, z) = \langle \mathbf{v}(z) \rangle + \mathbf{v}^*(x, y, z), \tag{2}$$

where $\langle \mathbf{v}(z) \rangle$ is the horizontally averaged Cartesian coordinate wind vector over a box 200 km on a side centered on the storm,

$$\langle \mathbf{v}(z) \rangle = \iint \mathbf{v}_s(x, y, z)\, dx\, dy. \tag{3}$$

This variable provides an approximation of the environmental flow around the storm (Marks et al. 1992). The vector $\mathbf{v}^*(x, y, z)$ in (2) represents the flow associated with the vortex itself. The vortex wind field $\{\mathbf{v}^*(x, y, z)\}$ in (2) is then interpolated from Cartesian to cylindrical coordinates $\{\mathbf{v}^*_{\text{cyl}}(r, \lambda, z)\}$.

Taking advantage of the circular symmetry of the horizontal storm-relative winds, $\mathbf{v}^*_{\text{cyl}}(r, \lambda, z)$ may be decomposed into two components:

$$\mathbf{v}^*_{\text{cyl}}(r, \lambda, z) = \overline{\mathbf{v}}(r, z) + \sum_{i=1}^{n} \upsilon'_i(r, \lambda, z), \tag{4}$$

where $\overline{\upsilon}(r, z)$ is the azimuthally averaged component of the hurricane vortex and $\upsilon'_i(r, \lambda, z)$ represents the deviation of $\overline{\upsilon}(r, z)$ from $\boldsymbol{\upsilon}^*_{\text{cyl}}(r, \lambda, z)$. In terms of a Fourier decomposition, $\overline{\upsilon}(r, z)$ corresponds to the wavenumber-0 component of the vortex flow and $\upsilon'_i(r, \lambda, z)$ corresponds to the remainder of the perturbation wind, that is, that part not accounted for by the environmental flow or the symmetric vortex (i.e., wavenumbers 1 and higher, with n representing the maximum number of wavenumbers considered). The subscript i in (4) refers to the wavenumber. In the analyses presented here, wavenumbers 0 and 1 are considered (i.e., $n = 1$). A similar Fourier decomposition was applied to other fields, such as vertical motion and model-derived reflectivity.

3. Observed characteristics of Hurricane Bonnie

a. Synoptic evolution

The origin of Bonnie can be traced to a vigorous tropical wave that moved off the African coast on 14 August. At that time, the wave was characterized by a broad low- and midlevel cyclonic circulation that tracked west-southwestward under the influence of a strong subtropical ridge. As the system reached warmer ocean temperatures in the central Atlantic, it became better organized and was named a tropical depression at 1200 UTC 19 August. The depression continued to move around a strong Bermuda high, tracking toward the west-northwest and reaching tropical storm strength at 1200 UTC 20 August (Fig. 2). Figure 3 shows the 850- and 200-hPa heights and winds at 0000 UTC 22 August. A broad ridge extends in the low levels from the eastern United States into the Atlantic Ocean, supporting broad easterly flow over Bonnie. In the upper levels an anticyclone is nearly coincident with the storm. Under these favorable winds, Bonnie strengthened to hurricane status at 0600 UTC 22 August.

Bonnie continued to strengthen, reaching a minimum central pressure of 954 hPa at 0000 UTC 24 August. By 0000 UTC 25 August, the hurricane was on the western side of the Bermuda high (Fig. 4), tracking northwestward. In the upper levels (Fig. 4a), a trough axis extended down along the East Coast to the western side of Bonnie. A day later, this upper-level trough axis retrograded to the west to become centered off the west coast of Florida (Fig. 4b). The storm approached the North Carolina coast, passing onshore just east of Cape Fear at 2130 UTC 26 August with a minimum sea level pressure of 963 hPa and surface winds of $\sim$50 m s^{-1}.

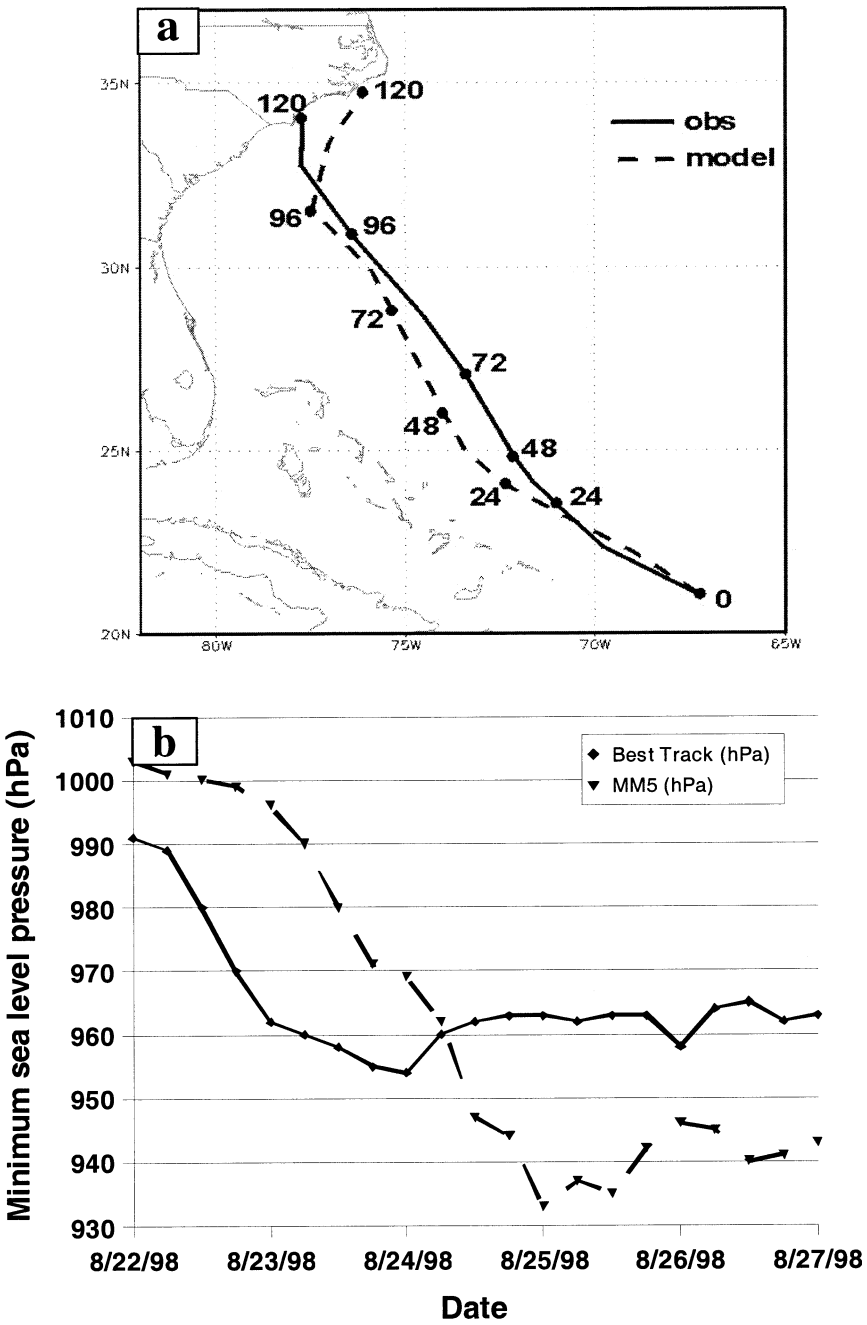

FIG. 2. (a) Plot of simulated track (dashed) vs best track (solid) for Hurricane Bonnie between $t = 0$ h and $t = 120$ h (i.e., between 0000 UTC 22 Aug and 0000 UTC 27 Aug). (b) Plot of simulated minimum sea level pressure (dashed) vs best track pressure (solid) between 0000 UTC 22 Aug and 0000 UTC 27 Aug.

The storm subsequently turned to the northeast across eastern North Carolina and headed out to sea.

An examination of the environmental flow fields later in the life of Bonnie (0000 UTC 25 and 26 August; Fig. 4) shows an evolving pattern of directional shear. At 0000 UTC 25 August the low-level flow around the western side of the Bermuda high was from the south-southeast. In the upper levels, the flow over the storm was from the west to west-northwest because of the proximity to the axis of the upper-level trough. This produced significant directional shear from the west to west-northwest. Twenty-four hours later, after the upper-level trough moved westward and the storm tracked toward the northwest, the upper-level flow over the

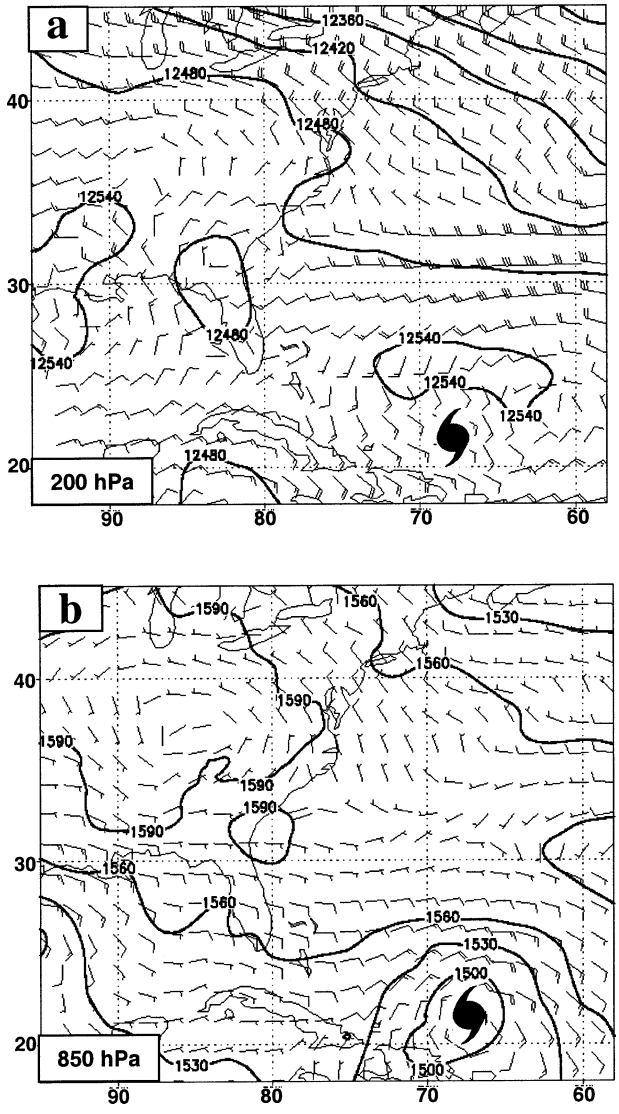

FIG. 3. Plot of NCEP 1° analyses of geopotential height (m, contours) and winds (barbs, m s^{-1}) at (a) 200 and (b) 850 hPa for 0000 UTC 22 Aug. Hurricane symbol denotes location of storm.

storm was from the south to south-southeast. Since this direction is very similar to that of the low-level flow the shear is predominantly along track.

b. Precipitation characteristics

The distribution of precipitation and its changes over time are shown in Fig. 5. Figure 5 shows radar composites taken from the National Oceanic and Atmospheric Administration's (NOAA) P-3 aircraft at different times during the life of the storm. At around 0000 UTC 25 August (Fig. 5a), when the storm was near the axis of the upper-level trough and experiencing considerable directional shear (cf. Figs. 4a–c), the reflectivity pattern was asymmetric, with reflectivities confined to the eastern and northeastern sides of the storm. The western side of the storm is nearly devoid of any radar echoes. Nearly 2 days later (1400 UTC 26 August; Fig. 5b), when the storm is approaching the coast and experiencing weaker shear (cf. Figs. 4b–d), the reflectivity distribution shows the presence of concentric eyewalls. The inner eyewall, about 20 km from the center, is confined to the northwest side of the storm. A broad outer eyewall, about 60–70 km from the center, wraps from the north side of the storm cyclonically around to the southeast side of the storm. Convection is more symmetrically distributed around the storm at this time than it was 2 days earlier.

These observations clearly show that the azimuthal distribution of precipitation changed over time, and that these changes occurred in an environment of changing large-scale flow fields encountered by the storm. Furthermore, the features described above were persistent, so that, for example, the wavenumber-1 reflectivity asymmetry shown in Fig. 5a lasted for many hours. Persistence in the distribution of clouds and precipitation has been observed in hurricanes for many years (e.g., Malkus et al. 1961; Marks 1985). The extent to which the distribution and evolution of precipitation is related to the evolution of the environmental vertical shear is the subject of the remainder of this paper.

4. Simulation results

The following section will begin with a description of the simulated storm and its environment and a comparison with the observations. The emphasis is not on the model's reproduction of the life cycle of the storm. Common deficiencies in current models, such as the initial vortex structure and uncertainties in the physical parameterizations of surface fluxes and microphysics, make the simulation imperfect. The emphasis here will be on gaining meaningful insight into the physical processes occurring in the model that are responsible for producing the distribution of precipitation.

The subsequent subsections will focus on the evolution of the environmental vertical shear and its relation to the vortex structure and reflectivity pattern. The discussion in these subsections will focus on the period between 0000 UTC 25 August and 0000 UTC 27 August (72–120 h in the simulation). This is when the highest-resolution mesh is active, and the ability to resolve fine-scale processes is greatest.

a. Description of simulated storm and comparison with observations

A comparison between the best track and simulated track and intensity is shown in Fig. 2. During the first 72 h, when the four-dimensional data assimilation on the outer mesh is active, the across-track error in the simulated storm motion is small; however, the simulated storm moves faster than the observed storm, and after 72 h it is about 300 km northwest of the actual location.

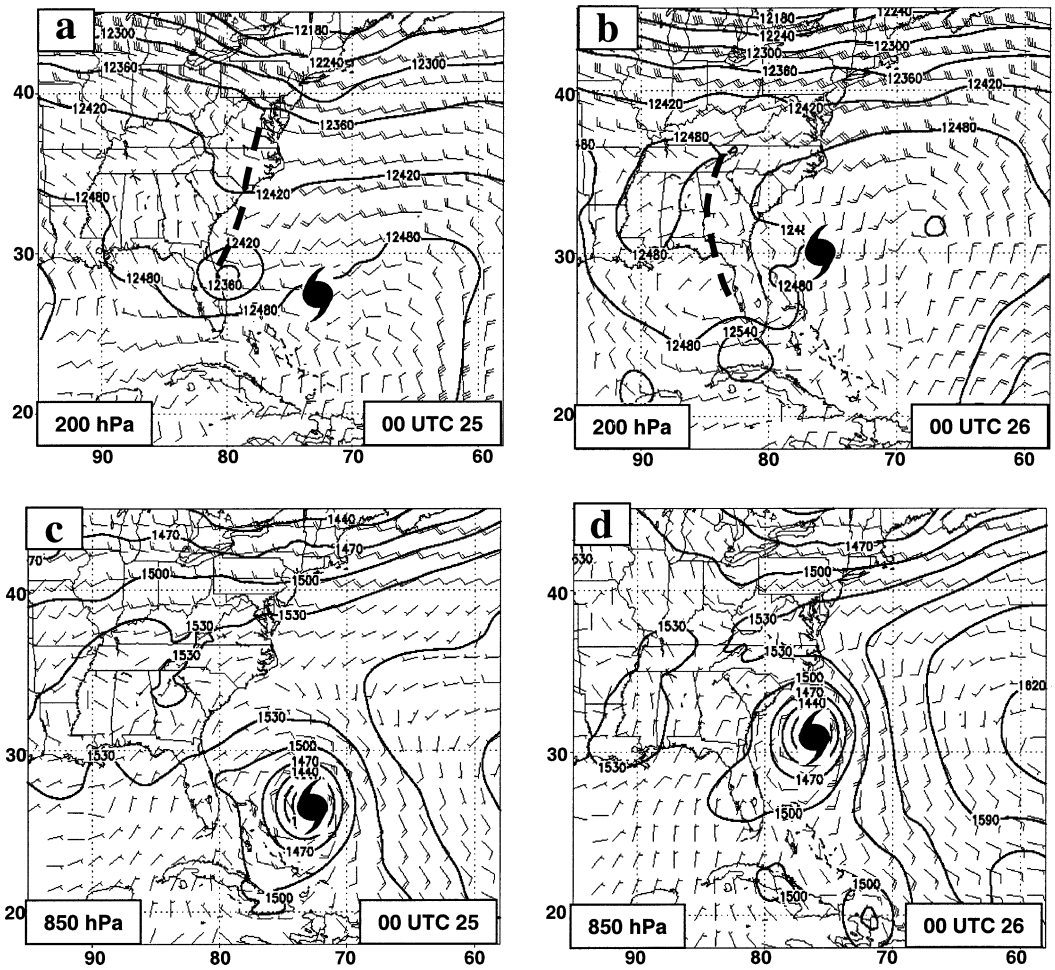

FIG. 4. Plot of NCEP 1° analyses of geopotential height (m, contours) and winds (barbs, m s^{-1}) at (top row) 200 and (bottom row) 850 hPa at (b), (d) 0000 UTC 26 Aug and (a), (c) 0000 UTC 25 Aug. Hurricane symbol denotes location of storm; bold dashed line in (a) and (b) denotes location of upper-level trough.

Both the simulated and the actual storms continue toward the northwest for the next 24 h, but at the 96-h simulation time the upper-level anticyclone to the southeast of the storm is stronger in the simulation than in the observations (cf. Figs. 4b and 6b). Consequently, upper-level southwesterly flow is stronger in the simulation, and the simulated storm turns sharply toward the north-northeast. This motion is in contrast to the real storm, which continued northwestward and then northward. Thus, the simulated storm recurves earlier than the actual storm, reaching the edge of the North Carolina Outer Banks near Cape Hatteras. Despite these differences, the location of the simulated storm at 120 h is only about 150 km from the observed.

A time series of simulated sea level pressure versus observed intensity (Fig. 2b) shows that the initial vortex (obtained from the NCEP global analysis) is weaker than the observed vortex. As a result, the simulated storm is weaker for the first 48 h. This is a common problem with simulations that use initial vortices derived from global models, as was recognized in Kurihara et al. (1993) and Xiao et al. (2000). After 48 h, when the observed storm reached its lowest pressure, the simulated storm continues to deepen. The observed storm leveled off after reaching a minimum central pressure of 960 hPa, while the intensity of the simulated storm continues to deepen until 72 h of simulation time, when the central pressure reaches 940 hPa. Likely reasons for the overdeepening of the simulated storm include the lack of any coupling with the ocean and shortcomings in the representation of surface fluxes of heat and moisture at high wind speeds.

Comparison of the large-scale flow fields shows that the model reproduces the environmental flow reasonably well. Figure 6 shows the 850- and 200-hPa height and wind fields at 0000 UTC 25 and 26 August. The simulated low-level flow fields compare favorably with the model analyses at both times (cf. Figs. 4 and 6): the flow is from the southeast and southsoutheast as the storm continues around the western

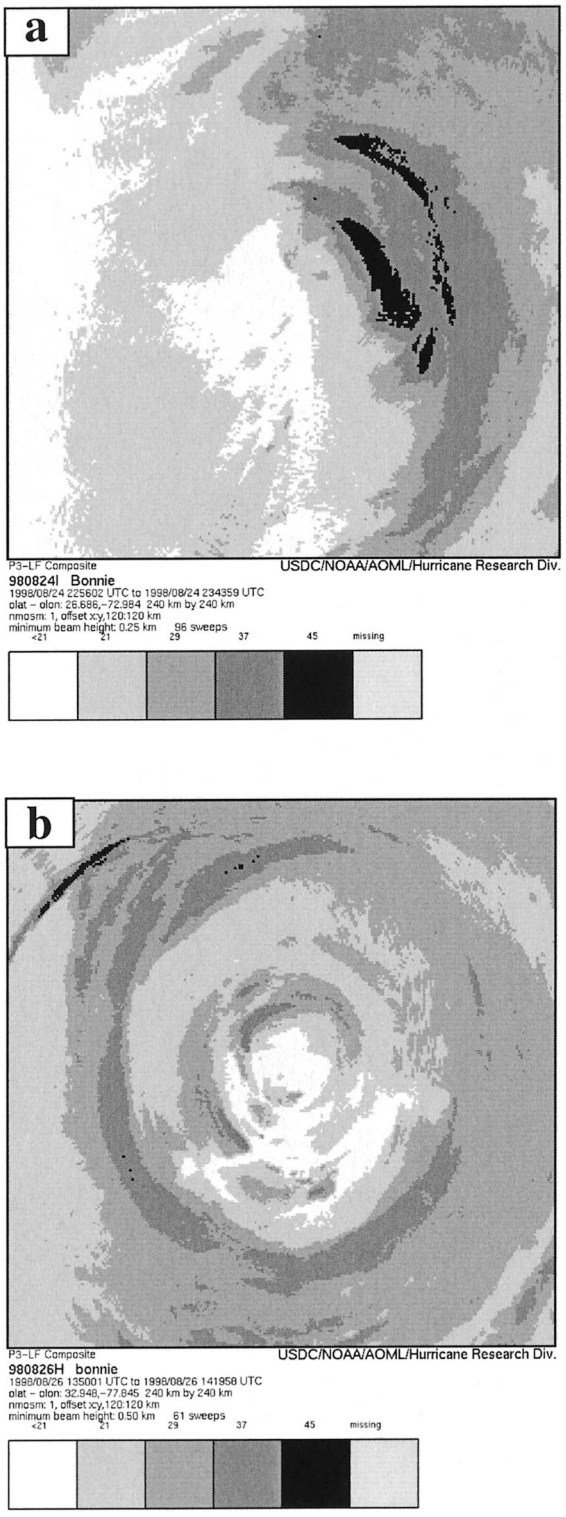

FIG. 5. Radar composites from the NOAA P-3 aircraft. (a) Composite from 2256 to 2344 UTC 24 Aug at an altitude of 1508 m. (b) Composite from 1350 to 1420 UTC 26 Aug at an altitude of 3533 m. Size of domains in both figures is 240 km × 240 km.

edge of the Bermuda high. In the upper levels, the axis of the simulated trough is displaced about 300 km to the west of the observed location. Given that the simulated storm is farther northwest than the observed (Fig. 2), however, the simulated storm is in a similar location relative to the trough axis. Thus, predominantly southwesterly and west-southwesterly upper-level winds below over the simulated storm, producing directional shear with the low-level flow, in agreement with the model analyses. By 0000 UTC 26 August, the upper-level trough has closed off to become a cutoff low near the observed closed circulation. The simulated storm is to the east of this cutoff low, putting it under predominantly south-southwesterly flow and weaker directional shear. This pattern is consistent with the model analyses.

Reflectivity fields calculated from the model's hydrometeor fields (Fig. 7) show that the model does a reasonably good job at capturing the changes in the azimuthal distribution of precipitation with time. Figure 7a shows model-derived reflectivity at the $\sigma = 0.844$ level (about 1500 m) at 0200 UTC 25 August. The figure shows a pronounced wavenumber-1 structure in reflectivity in the core region. High reflectivities are confined to the northern and northeastern sides of the storm. To the south and southwest the reflectivities drop off substantially. A comparison of this figure with the P-3 radar image a couple of hours earlier (Fig. 5a) shows rough agreement in terms of the azimuthal distribution of reflectivity, with both the observations and the simulation showing the reflectivity maximum in approximately the same azimuthal location. Later in the storm's evolution, the model produces two reflectivity maxima, about 60 km from the storm's center, on the northwest and southeast sides of the storm (Fig. 7b), in agreement with the locations of the reflectivity maxima shown in Fig. 5b. Furthermore, the model shows an inner eyewall about 20–30 km from the center on the western and southern sides of the storm. The model reflectivities in the core are higher and more widespread than those observed by the P-3 radars, though. Similar relationships between model-derived reflectivity and airborne- and ground-based radar observations have been found in other tropical cyclone simulations (e.g., Liu et al. 1997), and they likely arise due to coarse resolution of the model and in the parameterization of surface fluxes and microphysical processes as well as possible calibration errors of the P3 radars.

b. Environmental vertical shear

As discussed above, both the observations and the simulation show that Hurricane Bonnie experienced a change from strong across-track shear (0000 UTC 25 August) to weaker along-track shear (0000 UTC 26 August). Figure 8 shows a time series of the magnitude and direction of the environmental shear be-

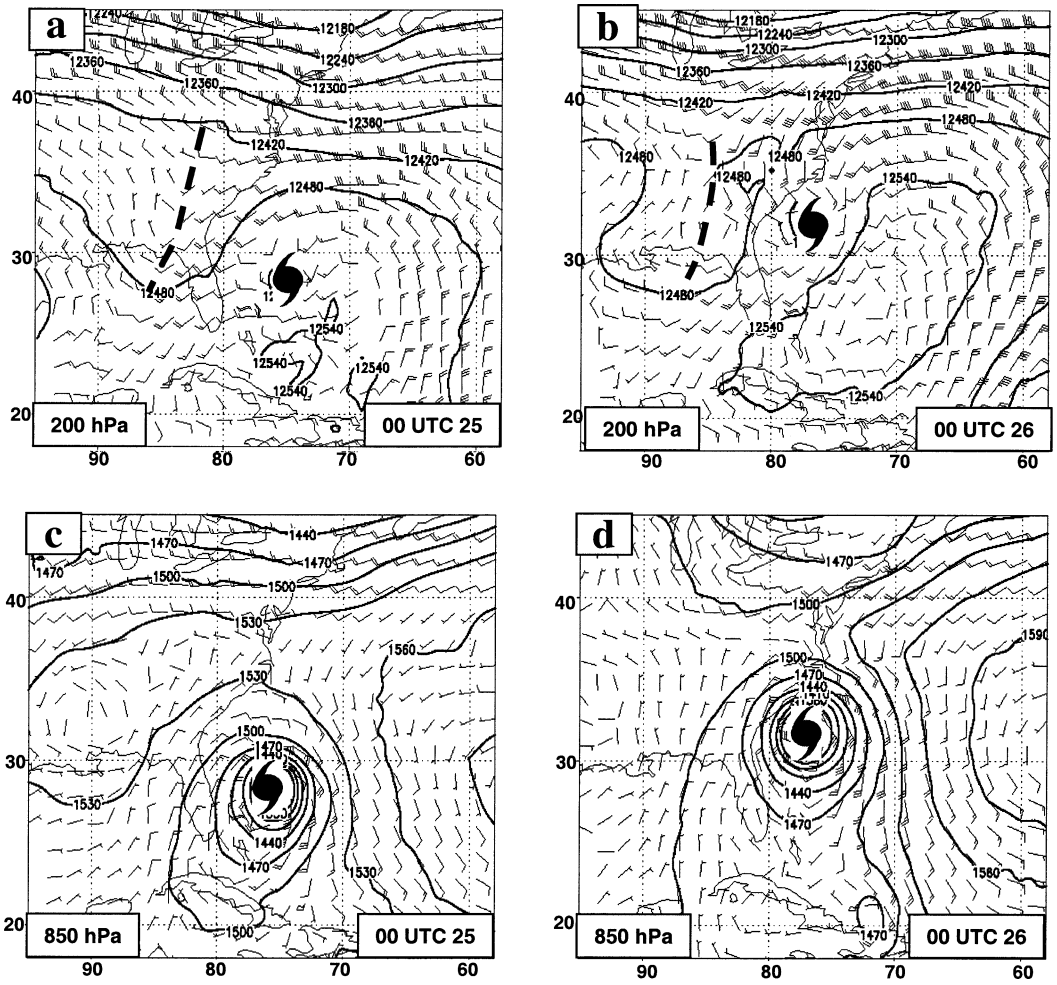

FIG. 6. Plot of simulated geopotential height (contours, m) and winds (barbs, m s^{-1}) at (top row) 200 and (bottom row) 850 hPa for (a), (c) 0000 UTC 25 Aug and (b), (d) 0000 UTC 26 Aug. Hurricane symbol denotes location of storm; bold dashed line in (a) and (b) denotes location of upper-level trough.

tween 900 and 400 hPa[1] (i.e., $\langle \mathbf{v}_{400\text{hPa}} \rangle - \langle \mathbf{v}_{900\text{hPa}} \rangle$) from 0000 UTC 25 August through 0000 UTC 27 August. The shear is strong at the beginning of the time series, with values between 20 and 25 m s^{-1} for several hours. At 2100 UTC on 25 August, the shear drops significantly, reaching values between 5 and 10 m s^{-1} by 0300 UTC 26 August. The magnitude of the shear stays within this range until the end of the simulation at 0000 UTC 27 August. The direction of the shear shows a similar variation with time. At the beginning of the period the shear is from the west-southwest. This direction persists for about 18–21 h. It becomes more southwesterly and then predominantly south-southwesterly by about 1200 UTC 26 August. The shear during the first 24–30 h of the time series is primarily across track, as the storm moves toward the northwest in the presence of southwesterly shear. After 0000 UTC 26 August, when the storm moves north-northeast, the shear is along track.

c. Vortex wind fields

Figure 9 shows a plot of the azimuthally averaged component of the tangential and radial winds ($\overline{v}_t$ and $\overline{v}_r$) at 0600 UTC 25 August, when the shear is strong and across track, and 1800 UTC 26 August, when the shear is much weaker and along track. The symmetric circulations are stronger earlier in the time period. Maximum tangential winds exceed 45 m s^{-1} between 30- and 50-km radius from 900 to 750 hPa. Symmetric inflow in the boundary layer exceeds 12–14 m s^{-1}. Just inside the eyewall, at 20-km radius, there is a return flow outward of more than 4 m s^{-1} at 800 hPa, and a much broader region of outward motion in the

[1] While conventionally the 850–200-hPa layer is used to determine environmental shear, 400 hPa is used as the top of the layer in this study because the vortex center becomes harder to locate using the simplexlike algorithm here. Such a concern was also discussed in Reasor et al. (2000).

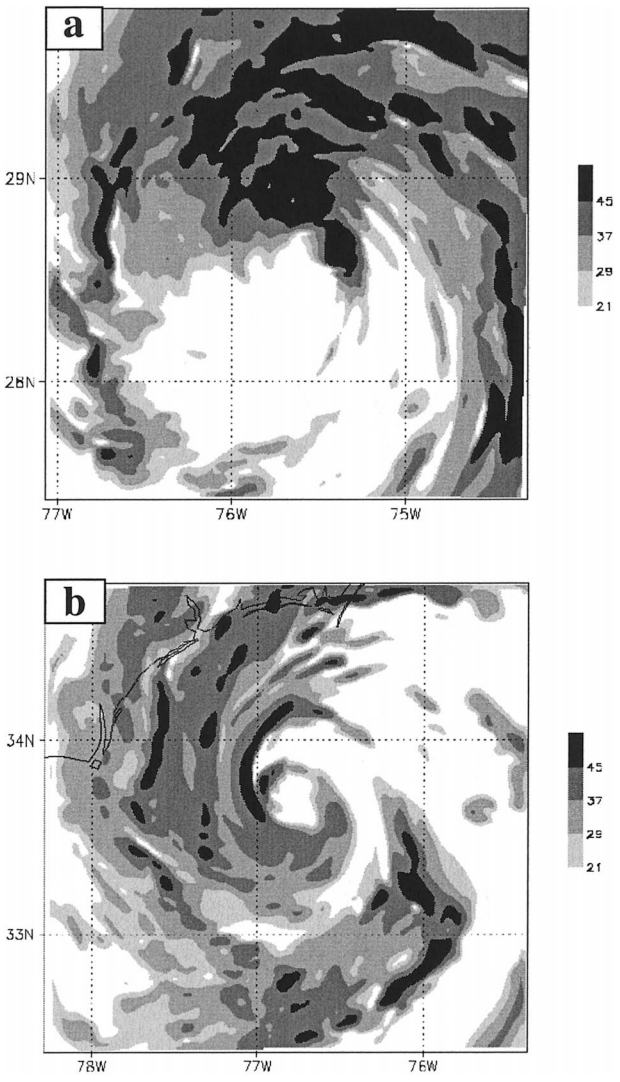

FIG. 7. Plot of simulated reflectivity (shaded, dBZ) at (a) 0200 UTC 25 Aug at $\sigma = 0.844$ level (1389 m) and (b) 1600 UTC 26 Aug at $\sigma = 0.665$ level (3238 m). Size of domains in both (a) and (b) is 267 km × 267 km.

upper troposphere above the eyewall. The simulated storm is at its most intense (cf. Fig. 2b) when the storm is over 30°C water (not shown). Thirty-six hours later, when the storm is over 28°C water (not shown), the symmetric circulations are weaker, with tangential winds >40 m s^{-1} over a narrow band between 20 and 40 km from 900 to 600 hPa. The low-level radial inflow is both shallower and weaker and the storm is less intense.

Total storm-relative tangential and radial flow (v_{ts} and v_{rs}) at 900 hPa is shown at 0600 UTC 25 August and 1800 UTC 26 August in Fig. 10. Tangential wind greater than 55 m s^{-1} is located on the northwest side of the storm at 0600 UTC 25 August. Inflow covers the entire eastern side of the storm, with maximum values greater than 30 m s^{-1} on the north-northeast side of the storm about 80 km from the center. Strong radial outflow occupies the southwest side of the storm. By 1800 UTC 26 August, the tangential wind is notably weaker, though there is still a maximum of 45 m s^{-1} on the west side of the storm. Radial inflow occurs in an arc that extends from the southeast side around to the northwest side. Maximum inflow, while weaker than at 0600 UTC 25 August, has shifted to the northwest side, and outflow (again weaker than before) is now on the south-southwest side.

d. Reflectivity and vertical shear

Changes in the wind patterns affect azimuth–height cross sections of reflectivity between 20–40-km radius at 0600 UTC 25 August and 1800 UTC 26 August (Fig. 11). A clear wavenumber-1 pattern is evident at 0600 UTC 25 August, with maximum values of reflectivity between the surface and 500 hPa beginning on the northeast and wrapping cyclonically around to the west side of the storm. A minimum in reflectivity, with some areas of no reflectivity, is evident on the south side of the storm. By 1800 UTC 26 August, the reflectivity is more symmetric, particularly below 800 hPa. There is some indication of a weak maximum on the west side, but the range in reflectivity values is much less than it had been 36 h before. A time–radius series of the wavenumber-0 and -1 components of the Fourier coefficients of reflectivity Z (i.e., $\overline{Z}$ and Z_1'; Fig. 12) shows that a sizable portion of the reflectivity signal between 20- and 40-km radius is projected onto the wavenumber-1 field between 0000 UTC 25 August and 0000 UTC 26 August. After 0000 UTC 26 August, the wavenumber-1 amplitude decreases while the wavenumber-0 coefficient amplitude increases, indicating that the reflectivity distribution is more symmetric.

Figure 13 shows the relationship between reflectivity and the shear of the environmental flow. The shear is obtained by plotting the hodograph of $\langle \mathbf{v} \rangle$ between 900 and 400 hPa. During the first 24 h the shear is strong (20–25 m s^{-1}) and predominantly from the west-southwest and southwest. At the same time the reflectivity in the core is greatest on the north side of the storm. This pattern resembles the downshear-left pattern described in observational studies by Willoughby et al. (1984), Marks et al. (1992), Franklin et al. (1993), and Gamache et al. (1997) and modeling studies of idealized storms by Frank and Ritchie (2001). At about 1800 UTC 25 August, the shear becomes more south-southwesterly, the reflectivity maximum moves to the northwest side of the storm, and the minimum moves to the southeast side as the storm begins to turn toward the northeast (cf. Figs. 2 and 13). By 0600 UTC 26 August, the shear is much weaker, ~5 m s^{-1}, and the reflectivity becomes more symmetric. This pattern continues until the end of the simulation.

Figure 14 confirms this relationship between shear and azimuthal distribution of reflectivity by showing a

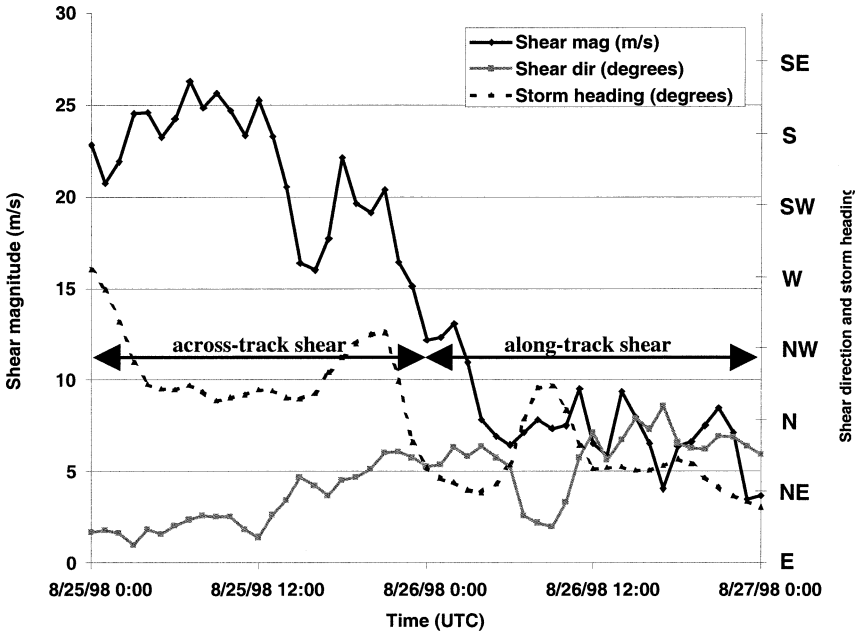

FIG. 8. Time series between 0000 UTC 25 Aug and 0000 UTC 27 Aug of the magnitude of 900–400-hPa wind shear (solid line; m s^{-1}), direction of 900–400-hPa wind shear (gray line; E means shear vector points toward the east, NW means shear vector points toward the northwest, etc.), and storm heading (dashed line; E means storm is heading toward the east, etc.) Periods of storm motion encountering across-track or along-track shear are indicated by arrows.

comparison of the time series of the magnitude of the vertical shear and the ratio between the wavenumber-1 and wavenumber-0 Fourier coefficients of reflectivity ($Z_1'/\overline{Z}$) between 20- and 40-km radius from 0000 UTC 25 August to 0000 UTC 27 August. Between 0000 and 2100 UTC 25 August the shear is 20–25 m s^{-1}. During this time the ratio of the wavenumber-1 to wavenumber-0 Fourier coefficients averages 80%. At 2100 UTC 25 August, the shear decreases to ~10 m s^{-1}. The ratio of the Fourier coefficients begins to decrease an hour or two after the shear begins its decrease. By 0600 UTC 26 August the shear is less than 10 m s^{-1} and the ratio of the coefficients is ~30%. Thus a substantial drop in the magnitude of the wavenumber-1 reflectivity asymmetry coincides with the decreasing shear.

e. Vortex tilt

As the foregoing discussion shows, the simulated distribution of reflectivity is well correlated with changes in the environmental flow. When the environmental shear is strong, the distribution of reflectivity is asymmetric. When the shear is weak, the reflectivity distribution becomes more symmetric. Previous studies suggest that vertical tilt of the vortex is one of the parameters that explains changes in the azimuthal distribution of convection (e.g., Jones 1995, 2000; Reasor et al. 2000). Figure 15 shows the location of the centers of circulation (as determined by the simplex algorithm described above) for every 100 hPa between 900 and 400 hPa for several times between 0000 UTC 25 August and 0000 UTC 27 August, with the vertical shear vector for the 900–400-hPa environmental wind superposed. During the entire period the vortex tilts generally downshear with height. Initially, the vortex tilts toward the east-northeast with height with a magnitude of about 15 km of tilt between 900 and 400 hPa. This is during the time when the shear is from the west-southwest with a magnitude of about 25 m s^{-1}. As the shear weakens and becomes more southwesterly and then south-southwesterly between 0000 and 0600 UTC 26 August, the tilt of the vortex generally decreases as the direction of the tilt is more toward the northeast. By the end of the time period, when the shear is on the order of 5 m s^{-1}, the vortex tilts generally toward the north, and the magnitude of the tilt is close to around 5 km.

Figure 16 shows a time series of the magnitude of this tilt superposed with the magnitude of the vertical shear. While the tilt magnitude is variable, a clear pattern emerges: tilt magnitudes are relatively large (between 10 and 15 km) during the first 24 h of the time series. Around 0000 UTC 26 August, after the environmental shear has begun to decrease, the tilt also begins to decrease. After 0600 UTC 26 August, tilts generally are between 5 and 10 km. The tilt began to decrease about 3 h after the shear began to decrease, though this timing is somewhat uncertain because of the variability in the tilt magnitude.

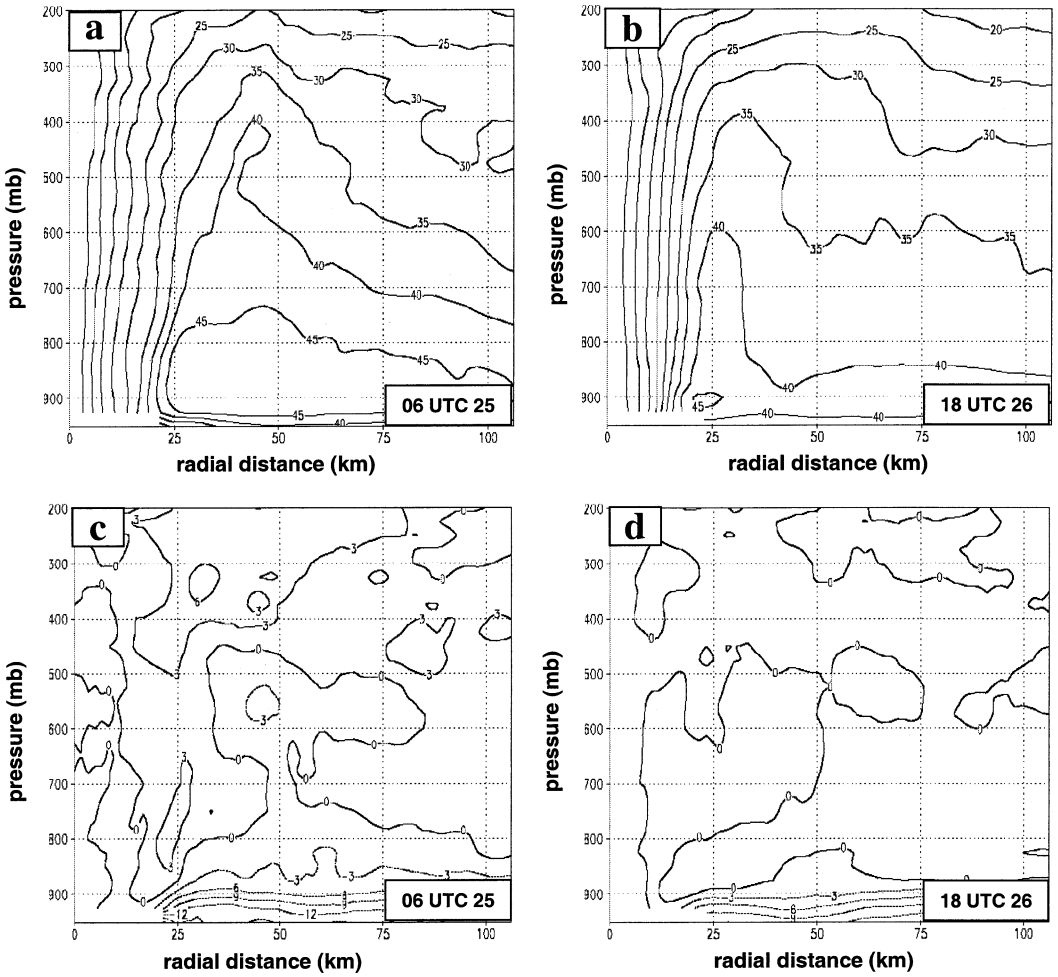

FIG. 9. Radius–height cross section of azimuthally averaged tangential wind (m s^{-1}; top row) and azimuthally averaged radial wind (m s^{-1}; bottom row) at (a), (c) 0600 UTC 25 Aug and (b), (d) 1800 UTC 26 Aug.

f. Boundary layer divergence and vertical motion

The relationship of the tilt of the vortex with boundary layer parameters such as divergence and vertical motion is shown in Figs. 17 and 18. Figure 17 shows the wavenumber-1 component of divergence $(\nabla \cdot \mathbf{V})_1'$ at 900 hPa at 0600 UTC 25 August and 1800 UTC 26 August. Superposed on this figure are the locations of the 900- and 400-hPa vortex centers and the distance between them. At 0600 UTC 25 August, the wavenumber-1 convergence is quite pronounced, with maximum values $< -1.2 \times 10^{-3}$ s^{-1} at an azimuth of 15°–30° from east. The vortex tilts nearly due east with height (around 5° of azimuth) and the magnitude of the tilt is 15 km. The maximum wavenumber-1 component of boundary layer convergence is located roughly underneath and downstream of the upper vortex center. By 1800 UTC 26 August, the divergence pattern shows a much weaker wavenumber-1 signal. The maximum value of convergence is now -0.3×10^{-3} s^{-1}. Furthermore, the location of the maximum has rotated counterclockwise to tilt toward the northeast with height at an azimuth of 45°. The tilt magnitude has decreased significantly to about 5 km.

The relation between boundary layer divergence and low-level vertical motion is shown in Fig. 18. The total vertical motion is averaged between the center of the storm and 25-km radius and between 900 and 800 hPa to produce low-level vertical motion as a function of azimuth. Even though averaging between the eye and the eyewall will reduce the upward motion signal and the model-generated vertical motion is dominated by high-frequency modes, a distinct signal arises (Fig. 18). First, the magnitude of the low-level upward motion is much greater at 0600 UTC 25 August, with values approaching 1 m s^{-1} in the northeastern quadrant of the storm. At 1800 UTC 26 August, there is still a region of upward motion, but the maximum values are less than half that at 0600 UTC 25 August. Both times show a minimum in vertical motion generally along the western and southern sides of the storm, but the 0600 UTC

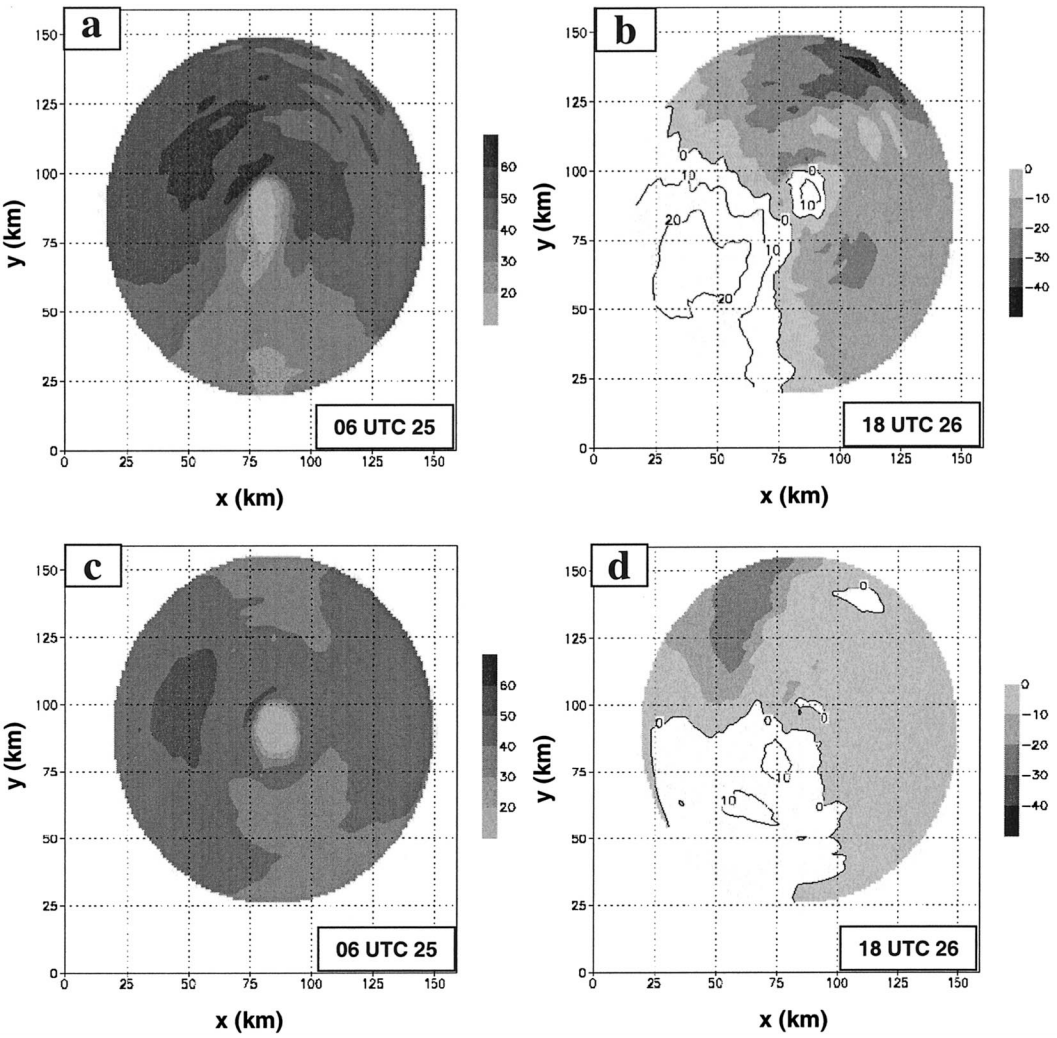

FIG. 10. Plot of 900-hPa storm-relative tangential (left column; shaded; m s^{-1}) and radial wind (right column; negative values shaded, positive values contoured; m s^{-1}) at (a), (c) 0600 UTC 25 Aug and (b), (d) 1800 UTC 26 Aug.

25 August profile shows downward motion over about 90° of azimuth (between the northwestern and southwestern quadrants), while the 1800 UTC 26 August profile only shows near-zero vertical motion over this area. At both times the upward motion peak is located downstream of the maximum in wavenumber-1 900-hPa convergence (cf. Figs. 18 and 19), consistent with the conceptual model of low-level convergence initiating updrafts that are wrapped cyclonically around the storm by tangential winds. Furthermore, the 1800 UTC 26 August vertical motion maximum is rotated about 30° counterclockwise from the 0600 UTC 25 August maximum, roughly consistent with the rotation of both the 900–400-hPa tilt axis (cf. Fig. 16) and the wavenumber-1 900-hPa convergence maximum (cf. Fig. 17).

g. Accumulated rainfall pattern

Figure 19 shows the total simulated rainfall from 0000 UTC 25 August to 00 UTC 27 August, with the storm track superposed. During the first 24 h, when the simulated storm moves toward the northwest and experiences strong across-track shear, the rainfall pattern is distributed more symmetrically across the storm track. During the second 24-h period, after the simulated storm has turned toward the north-northeast and is encountering weaker along-track shear, the rainfall shows a distinct maximum on the left side of the track, despite the fact that the reflectivity is distributed more symmetrically around the storm during this time (cf. Figs. 13, 14). An explanation for this apparent paradox is provided in the following section.

5. Discussion

In this simulation of Hurricane Bonnie, the azimuthal distribution of convection evolved during the 48-h period between 0000 UTC 25 August and 0000 UTC 27 August from a highly asymmetric pattern to one that

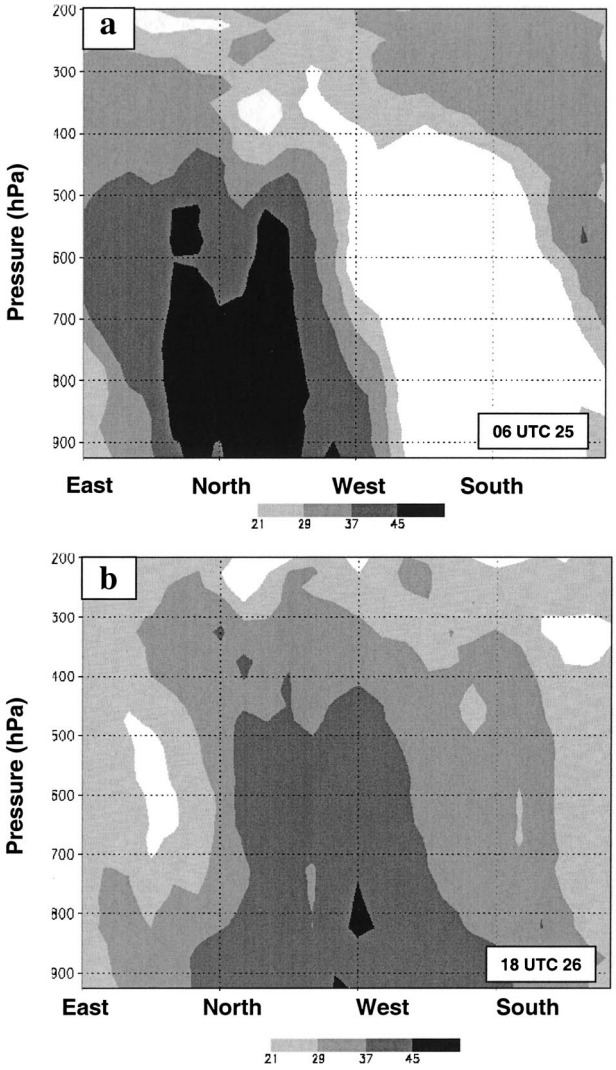

FIG. 11. Azimuth–height cross sections of reflectivity (shaded; dBZ) averaged between 20-and 40-km radius at (a) 0600 UTC 25 Aug and (b) 1800 UTC 26 Aug.

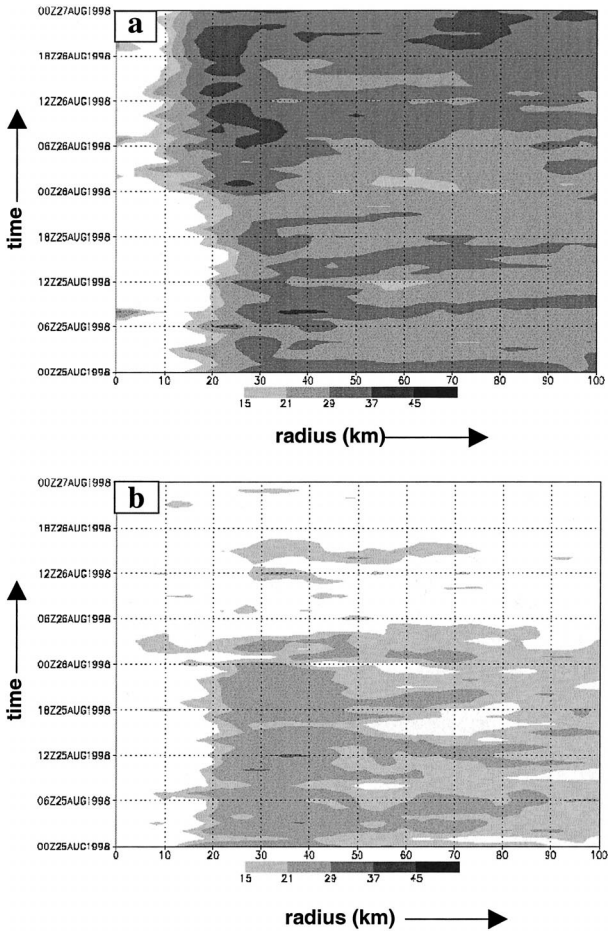

FIG. 12. Time–radius series of amplitude of Fourier coefficients of (a) wavenumber-0 reflectivity field (dBZ) and (b) wavenumber-1 reflectivity field (dBZ) between 0000 UTC 25 Aug and 0000 UTC 27 Aug. Radius is along the *x* axis, time increases along the *y* axis.

was more symmetric. Many studies have addressed the azimuthal distribution of convergence, vertical motion, and convection in the core of a storm. They have focused on asymmetries related with the translational speed of the storm and interactions of the storm with the environmental vertical shear. This study focuses on the role of vertical shear in governing the azimuthal distribution of convection. Changes in convection are well correlated with changes in the vertical shear. It remains a possibility, however, that changes in the distribution of convection are also related to changes in the translational speed and direction of the storm. Figure 20 shows a time series of the translational speed of the storm and the ratio of the wavenumber-1 and -0 Fourier coefficients of reflectivity between 0000 UTC 25 August and 0000 UTC 27 August. The translational speed of the simulated storm does show variability, ranging between 1.5 and 9.0 m s^{-1} during the 48-h time period. However, there is no systematic change in the speed over time, and certainly nothing that correlates as well with the changes in the azimuthal distribution of reflectivity as the environmental shear does. From these results it appears that, in this simulation, environmental shear is more important than storm translational speed in determining the azimuthal asymmetries in instantaneous rainfall.

The impact of the vertical shear on the structure of the vortex was addressed by looking at changes in the vertical tilt of the vortex and the accompanying changes in low-level divergence and vertical motion. At the beginning of the time period shown here the storm was already experiencing significant vertical shear on the order of 20–25 m s^{-1}. During this time the vortex showed a tilt of between 10 and 15 km, in roughly the downshear direction. As the shear dropped, the vortex tilt also decreased, starting a few hours after the decrease in shear. Even when the shear was relatively weak (at 5–10 m s^{-1}), the vortex continued to show a tilt of about

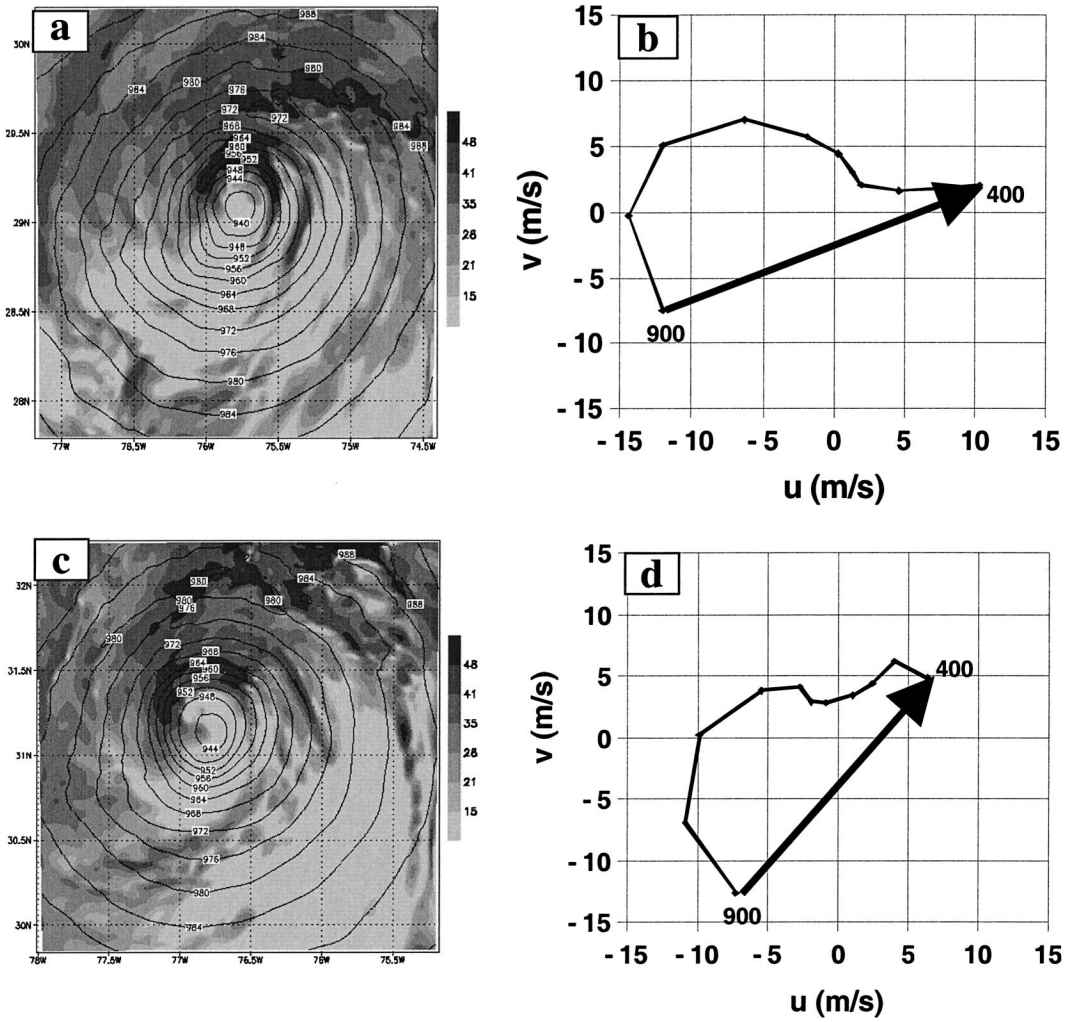

FIG. 13. Plots of simulated sea level pressure (left column; contour; hPa), reflectivity (left column; shaded; dBZ) at $\sigma = 0.844$ level, and hodograph of environmental winds between 900 and 400 hPa in vicinity of vortex (right column; m s^{-1}) at (a), (b) 0600 UTC 25 Aug, (c), (d) 1800 UTC 25 Aug, (e), (f) 0600 UTC 26 Aug, and (g), (h) 1800 UTC 26 Aug. Bold arrows in hodographs depict 900–400-hPa vertical shear vector.

5 km. The presence of this tilt even in relatively weak shear is in contrast to the results of Frank and Ritchie (2001), who did not show a significant tilt until the shear reached 15 m s^{-1}. Part of the reason why Frank and Ritchie did not see tilts with weaker shears (which they acknowledged) was that their use of a 5-km grid length could not resolve tilts much smaller than 10–15 km. However, as seen by this higher-resolution simulation and by observational studies such as Reasor et al. (2000) and Marks et al. (1992), tilts on the order of 5 km or less occur in weakly sheared hurricanes.

The fact that the direction of the vortex tilt stayed fairly well aligned in the downshear direction contrasts with some of the more idealized studies of Jones (1995, 2000), which show that the upper- and lower-level centers start to revolve around each other once the initial tilt occurs. There are several possible explanations (albeit speculative at this point) as to why the vortex in the simulation presented here does not appear to rotate about its midlevel center: First, the results presented in Jones (1995, 2000) are based on a model without diabatic processes. The simulation shown here does include convection, which would more strongly couple the upper- and lower-level regions of the vortex. Also, while it was not shown in the paper, the shear profile is highly variable with height, so the tilt of the vortex does not follow a simple linear shape with height. This complicates any possible interpretation regarding vertical penetration of the vortex momentum fields associated with the potential vorticity field. Finally, the magnitude of the shear diagnosed in the simulation is much stronger than the 3–6 m s^{-1} of shear imposed between 1 and 9 km in Jones (1995, 2000), so any forcing created by the self-induced flow created by the vortex tilt may be weaker, relative to the forcing created by the vertical shear, in the simulation shown here. Further diagnostic anal-

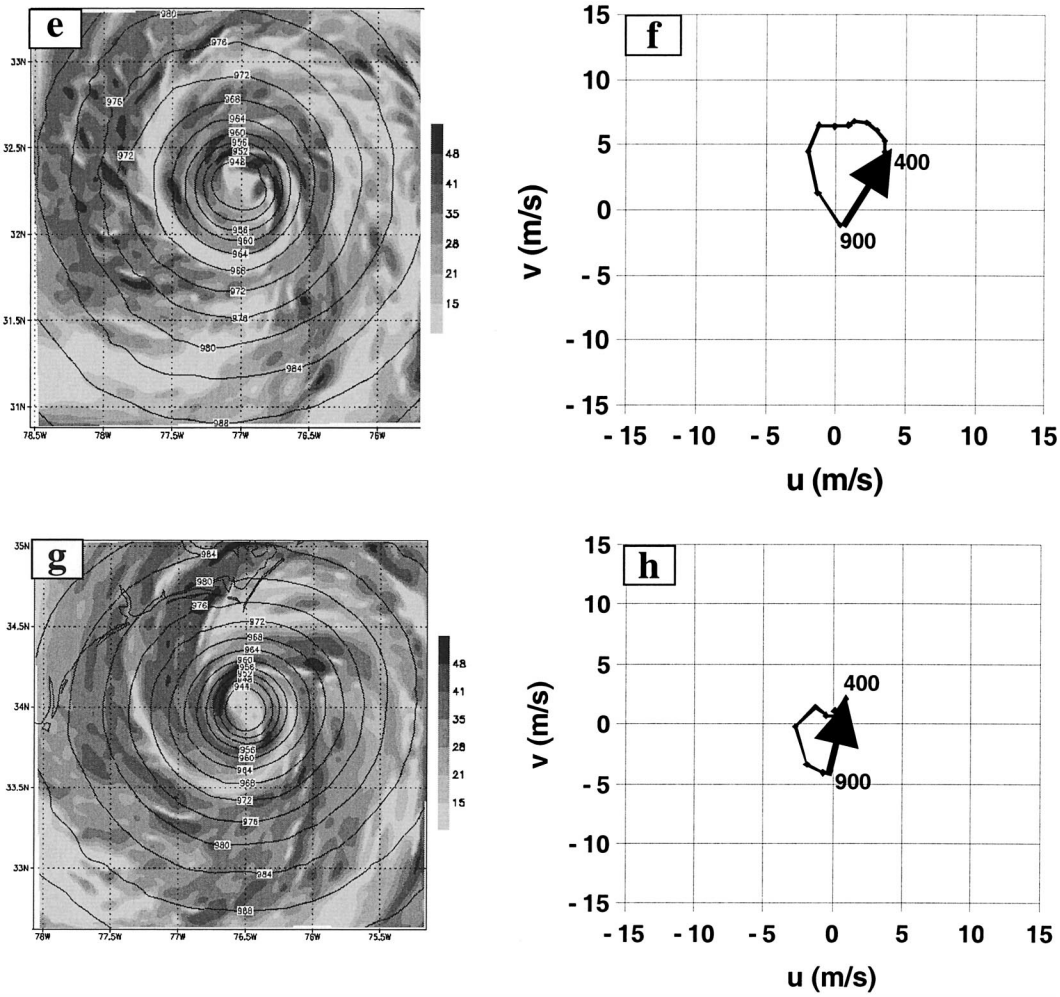

FIG. 13. (*Continued*)

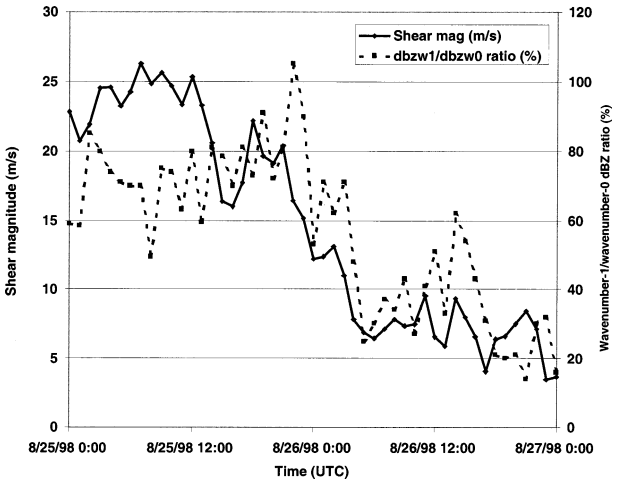

FIG. 14. Time series from 0000 UTC 25 Aug to 0000 UTC 27 Aug of the magnitude of the 900–400-hPa wind shear (solid line; m s^{-1}) and ratio of the amplitude of the Fourier coefficients of the wavenumber-1 and wavenumber-0 reflectivity fields (dashed line; %).

yses are needed to more accurately determine the reason for the differences between this simulation and the work of Jones (1995, 2000).

Another important question to address is the timing of changes in the tilt in relation to changes in the azimuthal distribution of rainfall. In this simulation tilt clearly changes rapidly in response to changes in the vertical shear. It was not clear-cut, however, that the changes in the shear *preceded* the changes in the tilt, nor is it clear that the azimuthal distribution of reflectivity changes prior to the reduction in tilt (cf. Figs. 15 and 17). Frank and Ritchie (2001) found that their simulated vortex tilted after the development of rainfall asymmetries, though the difference in time between the asymmetries in rainfall and the development of the vortex tilt was 24–48 h, much longer than in this case. If reflectivity changes before tilt, then it is possible that the changes in tilt are driven by changes in the distribution of convective heating, rather than changes in the vertical shear. The differences in the timing of the changes in reflectivity and tilt in the Bonnie simulation

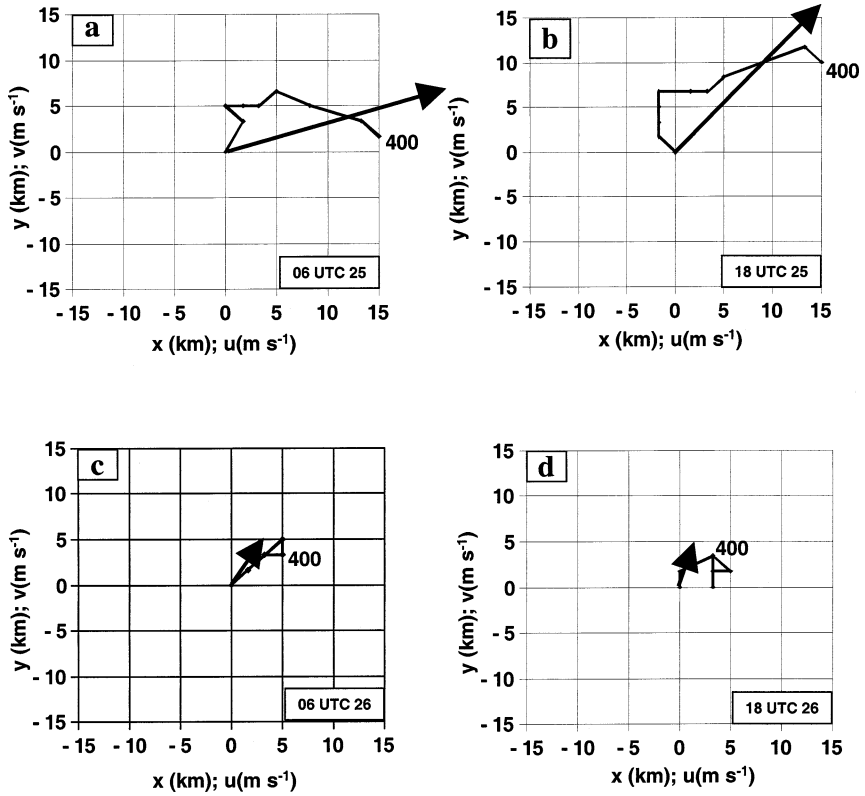

FIG. 15. Plot of displacement of vortex centers (solid line; km) between 900 and 400 hPa relative to location of 900-hPa center. Location of 900-hPa center is at (0,0) location of chart; location of 400-hPa center is denoted by ''400.'' Bold arrow depicts 900–400-hPa vertical shear vector (m s^{-1}; same scale). (a) 0600 UTC 25 Aug, (b) 1800 UTC 25 Aug, (c) 0600 UTC 26 Aug, (d) 1800 UTC 26 Aug.

are small, and could just reflect the different response times of convective triggering and vortex alignment to changes in the vertical shear. Further studies, with simulations of prescribed vortex structures and shear profiles at high resolution, are needed to adequately address this question.

While azimuthal asymmetries in model-derived reflectivity, low-level convergence, and vertical motion were all directly correlated with the magnitude of the vertical shear, the distribution of total accumulated rainfall in this case was not. The reason is related to the relationship between the direction of the shear vector and the storm track (Fig. 21). Between 0000 UTC 25 August and 0000 UTC 26 August, when the storm was moving toward the northwest, it was encountering strong across-track shear from the southwest. The shear was strong enough to create significant azimuthal asymmetries in the instantaneous rain rate on the downshear-left side of the shear vector (which at this time would be on the northwestern side of the storm). However, because the storm was heading toward the northwest, this asymmetry was concentrated in front of the storm, so that the accumulated rainfall was more or less equal on both sides of the track. When the storm turned toward the north-northeast after 0000 UTC 26 August, the shear vector became south-southwesterly, so that the storm experienced along-track shear. Since there was still vertical shear over the storm, albeit weaker than previously, there was still a preference for the downshear-left maximum in instantaneous rainfall. Because the storm was heading toward the north-northeast, the asymmetry caused the distribution of total accumulated rainfall to be concentrated on the left side of the track.

6. Summary and concluding remarks

In this study Hurricane Bonnie, which experienced significant vertical shear and exhibited a high degree of azimuthal asymmetries in reflectivity and rainfall, was simulated. The high-resolution numerical model reproduced the storm track and evolution of the azimuthal asymmetries reasonably well. The simulated storm was stronger than observed. Model biases are common in numerical simulations of tropical cyclones and reflect the limitations of the model initialization and parameterization of surface fluxes, ocean feedback, and microphysics. While the model did not perfectly reproduce the intensity evolution of Bonnie, the track and synoptic-scale environment were reasonably well represented. Thus, the evolution of the azimuthal asymme-

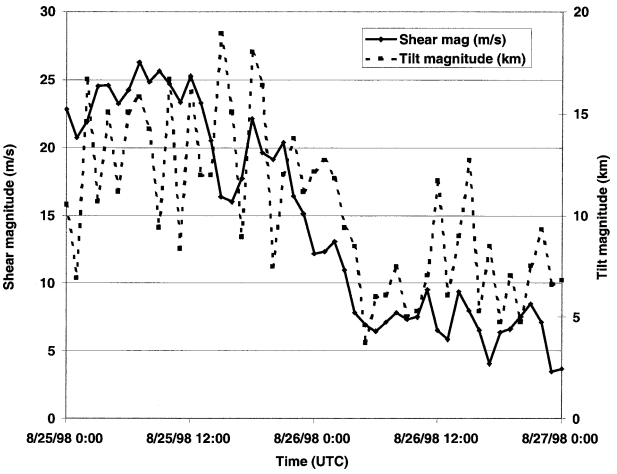

FIG. 16. Time series between 0000 UTC 25 Aug and 0000 UTC 27 Aug of the magnitude of the 900–400-hPa wind shear (solid line; m s^{-1}) and magnitude of the horizontal displacement of the 400-hPa storm center from the 900-hPa storm center (dashed line; km).

tries of reflectivity generally followed the observations, and the simulation reproduced reality well enough to justify a detailed examination of the physical processes in the model.

The vertical shear between 0000 UTC 25 August and 0000 UTC 26 August was between 20 and 25 m s^{-1} between 900 and 400 hPa, but decreased rapidly over a 6-h time period, so that it was between 5 and 10 m s^{-1} after 0300 UTC 26 August. Both symmetric and total winds showed that the storm was stronger at the beginning of this 48-h period, when the storm was over 30°C water, and weakened by the end of the time period. Radial inflow on the eastern and northern sides of the storm exceeded 30 m s^{-1}. The inflow rotated cyclonically and weakened, with maximum values around 15 m s^{-1} on the northwest side of the storm by 1800 UTC 26 August.

The distribution of model-derived reflectivity was closely related to both the magnitude and direction of the vertical shear vector. When the shear was strong, reflectivity in the core was located on the left side of the shear vector, and little occurred on the right side of the shear, in agreement with previous observational and modeling studies. As the shear weakened, the distribution of reflectivity became more symmetric. The change occurred essentially simultaneously with the change in shear.

The vortex exhibited a tilt from the vertical between 900 and 400 hPa that generally coincided with the direction of the shear vector. As the direction and magnitude of the shear changed, so did the direction and magnitude of the tilt vector. It changed from about 15 km toward the east when the shear was west-southwesterly at 20–25 m s^{-1} to about 5 km toward the northeast when the shear was south-southwesterly at 5–10 m s^{-1}. As with reflectivity, the changes in tilt also occurred simultaneously with the changes in vertical shear. The

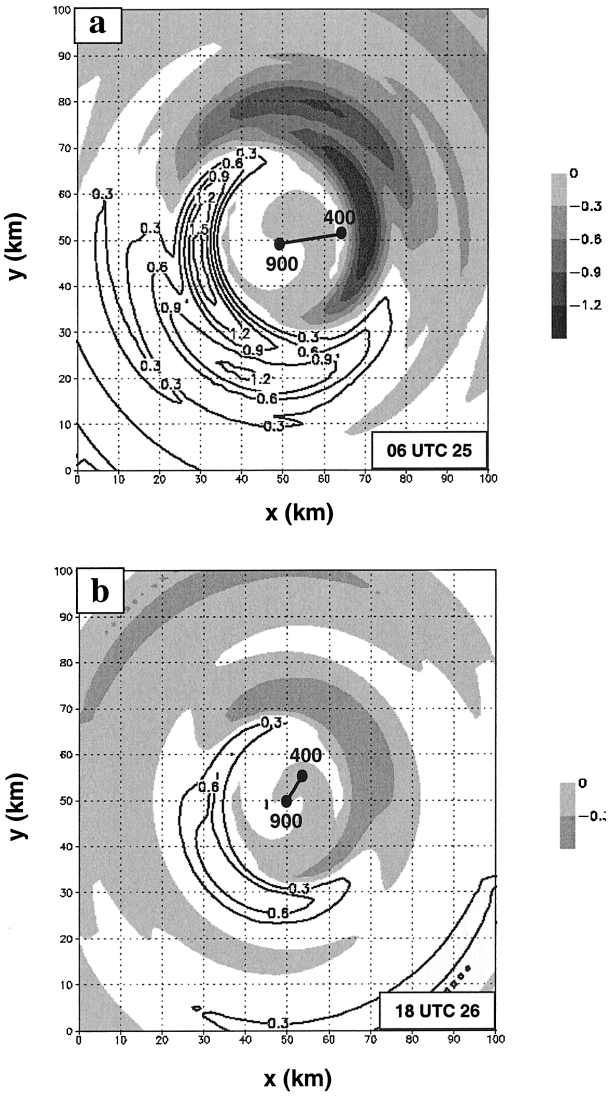

FIG. 17. Plot of amplitude of Fourier coefficient of wavenumber-1 divergence at 900 hPa ($\times 10^{-3}$ s^{-1}) at (a) 0600 UTC 25 Aug and (b) 1800 UTC 26 Aug. Positive values are contoured; negative values are shaded. Locations of 900-and 400-hPa centers are marked.

timing of these changes was more difficult to pinpoint since the vortex tilt was highly variable.

When the vortex had a pronounced tilt, the low-level divergence field showed a stronger wavenumber-1 asymmetry than when the vortex was more upright. The location of the maximum in low-level convergence was roughly underneath the upper-level circulation center. As the vortex tilt decreased, the wavenumber-1 divergence asymmetry also decreased, though its maximum remained underneath the upper-level circulation center. The azimuthal distribution of low-level vertical motion showed a pattern consistent with the wavenumber-1 pattern described above: upward motion was located downstream of the low-level convergence maximum, on the northeastern side of the storm at 0600 UTC 25 August

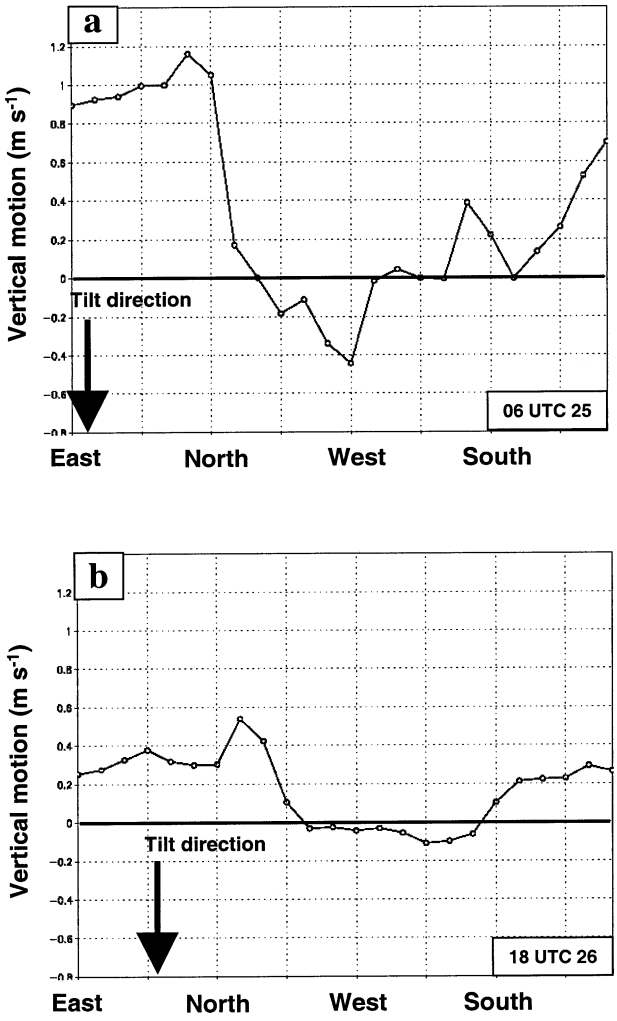

FIG. 18. Azimuthal distribution of vertical motion (m s^{-1}; 0 m s^{-1} line highlighted) averaged between 900 and 800 hPa between 0- and 25-km radius at (a) 0600 UTC 25 Aug, and (b) 1800 UTC 26 Aug. Direction of tilt of vortex between 900 and 400 hPa shown by arrow.

and on the northern side at 1800 UTC 26 August. On the western and southern sides of the storm vertical motion was either near zero or downward. The shift in the location of the upward motion maximum was consistent with the shift in both the axis of vortex tilt and the location of the low-level convergence maximum and the magnitude of the upward motion was stronger when the vortex tilt was greater.

While the magnitude of the azimuthal asymmetries of low-level convergence, vortex tilt, and instantaneous rain rates (i.e., radar reflectivity) were all directly correlated with the magnitude of the shear, the distribution of accumulated rainfall was related not only with the environmental shear vector, but with the storm motion as well. The accumulated rainfall had a more symmetric distribution across the track of the storm when the shear was strong and across track, but it showed a distinct maximum on the left side of the storm track when the

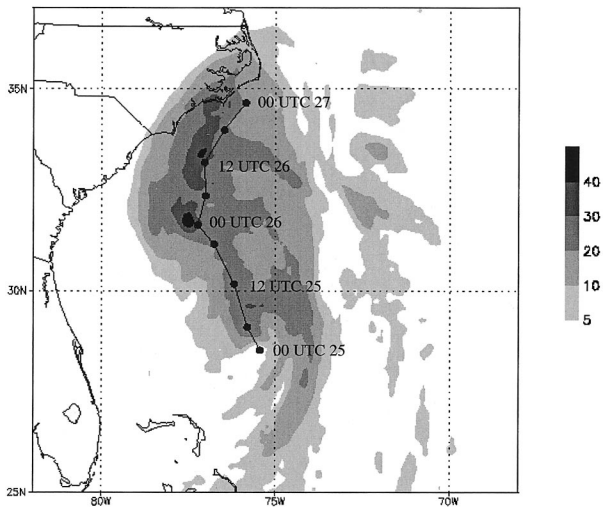

FIG. 19. Total accumulated rainfall (shaded; cm) between 0000 UTC 25 Aug and 0000 UTC 27 Aug. Track of simulated storm indicated by line; dots denote location of storm every 6 h.

shear was weak and along track. Such a relationship suggests a potentially useful forecast rule for total rainfall distribution. If the environmental shear and the storm track can be reliably forecast from the synoptic-scale flow fields, the qualitative distribution of total rainfall (across-track asymmetry versus uniformity) can be inferred. Since the amount of rainfall can be predicted from the expected translational speed of the storm (as is currently done operationally), more detailed rainfall forecasts may be possible by combining this algorithm with the across-track symmetry in the rainfall distri-

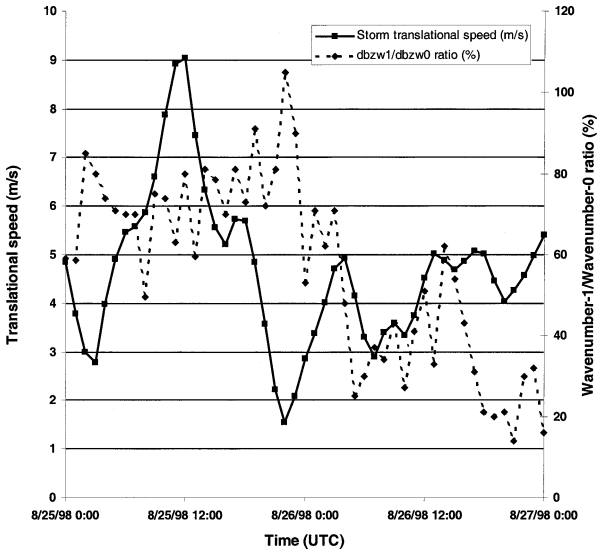

FIG. 20. Time series from 0000 UTC 25 Aug to 0000 UTC 27 Aug of the translational speed of the storm (solid line; m s^{-1}) and ratio of the amplitude of the Fourier coefficients of the wavenumber-1 and wavenumber-0 reflectivity fields (dashed line; %).

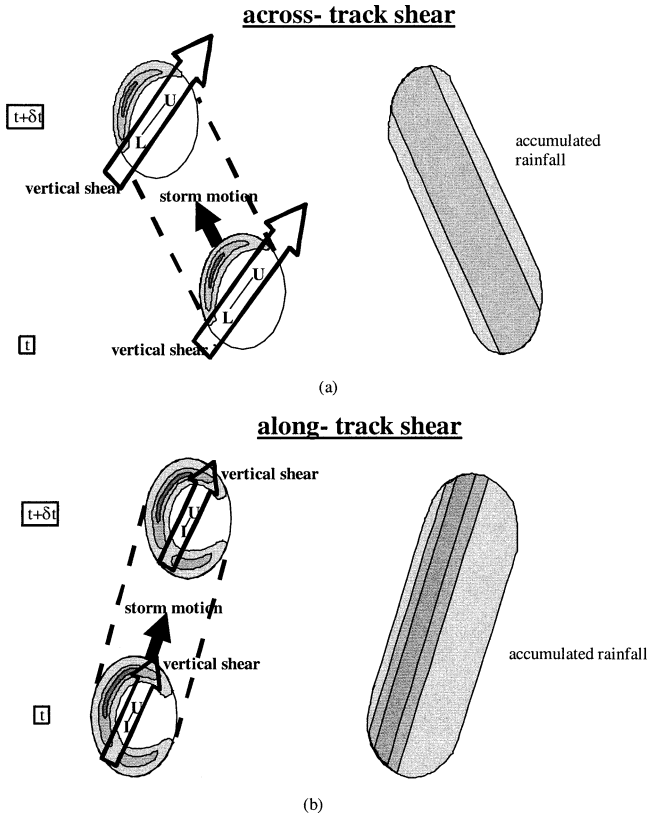

FIG. 21. Simplified schematic showing relationships between shear, storm heading, vortex tilt, instantaneous rainfall (reflectivity), and total rainfall. Shading in left column denotes reflectivity; increasingly dark shading indicates increasingly high reflectivity (i.e., rain rates). Shading in right column denotes total accumulated rainfall during δt time period; increasingly dark shading indicates increasingly heavy total rainfall amounts. Symbols L and U in left column denote locations of lower- and upper-level vortex centers, respectively. Thick solid arrow in left column indicates storm heading; thick transparent arrow in left column indicates vertical wind shear vector. (a) Across-track shear; (b) along-track shear.

bution. Analyses of numerous other cases are required, though, before a reliable algorithm could be developed.

An important question to address is how realistic this simulation is, and how it could be improved. As shown above, the simulated storm was more intense than the observed storm. Part of the reason for this is likely that the initial vortex was taken from global model analyses, so the vortex was poorly prescribed in the model. The radius of maximum winds was too large and the wind profile was too broad, so the subsequent evolution of the system was not completely realistic. Several techniques exist that attempt to improve the specification of the initial vortex (e.g., Kurihara et al. 1995; Xiao et al. 2000). Such techniques have often been used in 1) short simulations without an effective movable mesh and 2) real-time forecasts where a relatively long spinup time is not possible. In the simulation shown here, a 120-h simulation was possible due to the use of the movable mesh scheme. Consequently, the time period during which the analyses were performed (the final 48 h of the simulation) was sufficiently long after the model initial time that spinup has occurred, the storm has attained a balanced state in the simulation, and the storm has reached a steady-state intensity similar to (though stronger than) the observations. Therefore, even though the simulated storm is more intense than the observed storm, this discrepancy should not invalidate investigations of the physical mechanisms governing the impact of vertical on the azimuthal distribution of precipitation. Another likely source of error in the simulation is related to the fact that the sea surface temperatures were held constant throughout the simulation, even though observational studies show cooling under and behind tropical cyclones (Black 1983; Emanuel 1999; Cione et al. 2000; Bender and Ginis 2000) that feeds back to reduce the intensity of the tropical cyclone. To represent these feedbacks a coupled atmosphere–ocean–wave model is required. Such a model is currently under development, and once this coupled system is developed and tested, the simulation will be rerun and compared with the current configuration.

Another important area to address involves understanding the physical mechanisms underlying the development of these asymmetries. This study has merely shown relationships between shear, azimuthal rainfall asymmetries, and vortex tilt. There are several hypotheses that have been advanced in the literature to explain the development of these asymmetries, including examining the sources of asymmetric vertical motion in a tilted vortex (e.g., Jones 1995, 2000; Raymond 1992) and identifying vortex Rossby waves as being potentially key players (e.g., Reasor et al. 2000; Montgomery and Kallenbach 1997). In addition to the impact of vertical shear on the development of asymmetries, there is likely an impact of the presence of the landmass on the evolution of asymmetries as the storm approaches the shore. There is little doubt that the presence of land will affect the distribution of rainfall, both because of the reduced surface equivalent potential temperature from the inflowing air coming over the land and frictionally induced convergence that develops as onshore flow encounters the landmass. This paper was intended to isolate only one physical mechanism, environmental vertical shear, and evaluate its impact in governing the precipitation distribution of a simulation of Hurricane Bonnie. Other physical mechanisms, such as the interaction of a storm with land and topographical effects, were not the focus of this study. Further investigations that address these and other issues are certainly warranted.

Acknowledgments. The authors wish to thank Peter Dodge, John Gamache, Mark DeMaria, and an anonymous reviewer for their helpful comments on improving the manuscript; Frank Marks and Paul Reasor of HRD for their insightful discussions regarding the response of vortices in shear environments and explanations of the flow-field decomposition techniques; Shirley Murillo of HRD for her help in applying the simplex meth-

odology that was the basis for the technique used in the model analysis; Paul Leighton of HRD for providing the P-3 radar images; and Eric Uhlhorn of HRD for providing the code to perform the Fourier decompositions. This work was supported by NSF Grant ATM-9908944. This research was carried out (in part) under the auspices of the Cooperative Institute for Marine and Atmospheric Studies (CIMAS), a joint institute of the University of Miami and the National Oceanic and Atmospheric Administration, Cooperative Agreement NA67RJ0149.

REFERENCES

Bender, M. A., 1997: The effect of relative flow on the asymmetric structure of the interior of hurricanes. *J. Atmos. Sci.,* **54,** 703–724.

——, and I. Ginnis, 2000: Real-time simulation of hurricane–ocean interaction using a high-resolution coupled model: Effects on hurricane intensity. *Mon. Wea. Rev.,* **128,** 917–946.

Black, M. L., J. F. Gamache, F. D. Marks, C. E. Samsury, and H. E. Willoughby, 2002: Eastern Pacific Hurricanes Jimena of 1991 and Olivia of 1994: The effect of vertical shear on structure and intensity. *Mon. Wea. Rev.,* **130,** 2291–2312.

Black, P. G., 1983: Ocean temperature changes induced by tropical cyclones. Ph.D. dissertation, The Pennsylvania State University, State College, PA, 278 pp.

Blackadar, A. K., 1979: High-resolution models of the planetary boundary layer. *Advances in Environmental Science and Engineering,* J. Pfafflin and E. Ziegler, Eds., Vol. 1, No. 1, Gordon and Breach, 50–85.

Braun, S. A., and W.-K. Tao, 2000: Sensitivity of high-resolution simulations of Hurricane Bob (1991) to planetary boundary layer parameterizations. *Mon. Wea. Rev.,* **128,** 3941–3961.

Chen, S. S., W. Zhao, J. E. Tenerelli, R. H. Evans, and V. Halliwell, 2001: Impact of the AVHRR sea surface temperature on atmospheric forcing in the Japan/East Sea. *Geophys. Res. Lett.,* **28,** 4539–4545.

Cione, J. J., P. G. Black, and S. H. Houston, 2000: Surface observations in the hurricane environment. *Mon. Wea. Rev.,* **128,** 1550–1568.

Corbosiero, K. L., and J. Molinari, 2002: The effects of vertical wind shear on the distribution of convection in tropical cyclones. *Mon. Wea. Rev.,* **130,** 2110–2123.

DeMaria, M., 1996: The effect of vertical shear on tropical cyclone intensity change. *J. Atmos. Sci.,* **53,** 2076–2087.

Delsol, F., K. Miyakoda, and R. H. Clarke, 1971: Parameterized processes in the surface boundary layer of an atmospheric circulation model. *Quart. J. Roy. Meteor. Soc.,* **97,** 181–208.

Dudhia, J., 1989: Numerical study of convection observed during the Winter Monsoon Experiment using a mesoscale two-dimensional model. *J. Atmos. Sci.,* **46,** 3077–3107.

Emanuel, K. A., 1999: Thermodynamic control of hurricane intensity. *Nature,* **401,** 665–669.

Frank, W. M., and E. A. Ritchie, 1999: Effects of environmental flow upon tropical cyclone structure. *Mon. Wea. Rev.,* **127,** 2044–2061.

——, and ——, 2001: Effects of vertical wind shear on the intensity and structure of numerically simulated hurricanes. *Mon. Wea. Rev.,* **129,** 2249–2269.

Franklin, J. L., S. J. Lord, S. E. Feuer, and F. D. Marks Jr., 1993: The kinematic structure of Hurricane Gloria (1985) determined from nested analyses of dropwindsonde and Doppler radar data. *Mon. Wea. Rev.,* **121,** 2433–2451.

Gamache, J. F., H. E. Willoughby, M. L. Black, and C. E. Samsury, 1997: Wind shear, sea surface temperature, and convection in hurricanes observed by airborne Doppler radar. Preprints, *22d Conf. Hurricanes and Tropical Meteorology,* Fort Collins, CO, Amer. Meteor. Soc., 121–122.

Gray, W. M., 1968: Global view of the origin of tropical disturbances. *Mon. Wea. Rev.,* **96,** 669–700.

Grell, G. A., J. Dudhia, and D. R. Stauffer, 1994: A description of the fifth generation Penn State/NCAR Mesoscale Model (MM5) NCAR Tech. Note NCAR/TN-398 + STR, 138 pp.

Jones, S. C., 1995: The evolution of vortices in vertical shear: I: Initially barotropic vortices. *Quart. J. Roy. Meteor. Soc.,* **121,** 821–851.

——, 2000: The evolution of vortices in vertical shear: III: Baroclinic vortices. *Quart. J. Roy. Meteor. Soc.,* **126,** 3161–3185.

Kain, J. S., and J. M. Fritsch, 1993: Convective parameterization for mesoscale models: The Kain–Fritsch scheme. *The Representation of Cumulus Convection in Numerical Models, Meteor. Monogr.,* No. 46, Amer. Meteor. Soc., 165–170.

Kurihara, Y., M. A. Bender, and R. J. Ross, 1993: An initialization scheme of hurricane models by vortex specification. *Mon. Wea. Rev.,* **121,** 2030–2045.

——, ——, R. E. Tuleya, and R. J. Ross, 1995: Improvements in the GFDL hurricane prediction system. *Mon. Wea. Rev.,* **123,** 2791–2801.

Liu, Y., D.-L. Zhang, and M. K. Yau, 1997: A multiscale numerical study of Hurricane Andrew (1992). Part I: Explicit simulation and verification. *Mon. Wea. Rev.,* **125,** 3073–3093.

Malkus, J. S., C. Ronne, and M. Chafee, 1961: Cloud patterns in Hurricane Daisy, 1958. *Tellus,* **13,** 8–30.

Marks, F. D., Jr., 1985: Evolution of the structure of precipitation in Hurricane Allen (1980). *Mon. Wea. Rev.,* **113,** 909–930.

——, R. A. Houze Jr., and J. F. Gamache, 1992: Dual-aircraft investigation of the inner core of Hurricane Norbert. Part I: Kinematic structure. *J. Atmos. Sci.,* **49,** 919–942.

——, L. K. Shay, and PDT-5, 1998: Landfalling tropical cyclones: Forecast problems and associated research opportunities. *Bull. Amer. Meteor. Soc.,* **79,** 305–323.

Michalke, A., and A. Timme, 1967: On the inviscid instability of certain two-dimensional vortex-type flows. *J. Fluid Mech.,* **29,** 647–666.

Montgomery, M. T., and R. J. Kallenbach, 1997: A theory for vortex Rossby waves and its application to spiral bands and intensity changes in hurricanes. *Quart. J. Roy. Meteor. Soc.,* **123,** 535–565.

Neldar, J. A., and R. Mead, 1965: A simplex method for function minimization. *Comput. J.,* **7,** 308–313.

Peng, M. S., B.-F. Jeng, and R. T. Williams, 1999: A numerical study on tropical cyclone intensification. Part I: Beta effect and mean flow effect. *J. Atmos. Sci.,* **56,** 1404–1423.

Rappaport, E. N., M. Fuchs, and M. Lorenston, 1999: The threat to life in inland areas of the United States from Atlantic tropical cyclones. Preprints, *23d Conf. on Hurricanes and Tropical Meteorology,* Dallas, TX, Amer. Meteor. Soc., 811–814.

Raymond, D. J., 1992: Nonlinear balance and potential vorticity thinking at large Rossby number. *Quart. J. Roy. Meteor. Soc.,* **118,** 987–1015.

Reasor, P. D., M. T. Montgomery, F. D. Marks Jr., and J. F. Gamache, 2000: Low-wavenumber structure and evolution of the hurricane inner core observed by airborne dual-Doppler radar. *Mon. Wea. Rev.,* **128,** 1653–1680.

Shapiro, L. J., 1983: Asymmetric boundary layer flow under a translating hurricane. *J. Atmos. Sci.,* **40,** 1984–1998.

Stauffer, D. R., and N. L. Seaman, 1990: Use of four-dimensional data assimilation in a limited-area mesoscale model. Part I: Experiments with synoptic-scale data. *Mon. Wea. Rev.,* **118,** 1250–1277.

Tenerelli, J. E., and S. S. Chen, 2000: Vortex-following mesh refinement for simulating hurricanes with MM5. Preprints, *10th PSU/NCAR Mesoscale Model User's Workshop,* Boulder, CO, NCAR, 15–17.

Willoughby, H. E., 1988: Linear motion of a shallow-water barotropic vortex. *J. Atmos. Sci.,* **45,** 1906–1928.
——, F. D. Marks Jr., and R. J. Feinberg, 1984: Stationary and moving convective bands in hurricanes. *J. Atmos. Sci.,* **41,** 3189–3211.
Xiao, Q., X. Zou, and B. Wang, 2000: Initialization and simulation of a landfalling hurricane using a variational bogus data assimilation scheme. *Mon. Wea. Rev.,* **128,** 2252–2269.
Zhang, D.-L., and R. A. Anthes, 1982: A high-resolution model of the planetary boundary layer—Sensitivity tests and comparisons with SESAME-79 data. *J. Appl. Meteor.,* **21,** 1594–1609.